nature energy

Article

https://doi.org/10.1038/s41560-022-01179-3

Stalling oxygen evolution in high-voltage cathodes by lanthurization

Received: 9 February 2022

Accepted: 19 November 2022

Published online: 12 January 2023

Check for updates

Mingzhi Cai[1,10], Yanhao Dong[2,3,10], Miao Xie[4], Wujie Dong[4], Chenlong Dong[5], Peng Dai[6], Hui Zhang[7], Xin Wang[8], Xuzhou Sun[4], Shaoning Zhang[4], Moonsu Yoon[2], Haowei Xu[2], Yunsong Ge[1], Ju Li[2,9] ✉ & Fuqiang Huang[1,4] ✉

Coatings and surface passivation are sought to protect high-energy-density cathodes in lithium-ion batteries, which suffer from labile oxygen loss and fast degradations. Here we develop the theory underlying the high-voltage-induced oxygen evolution crisis and report a lanthurizing process to regulate the near-surface structure of energy materials beyond conventional surface doping. Using $LiCoO_2$ as an example and generalizing to Co-lean/free high-energy-density layered cathodes, we demonstrate effective surface passivation, suppressed surface degradation and improved electrochemical performance. High-voltage cycling stability has been greatly enhanced, up to 4.8 V versus Li^+/Li, including in practical pouch-type full cells. The superior performance is rooted in the engineered surface architecture and the reliability of the synthesis method. The designed surface phase stalls oxygen evolution reaction at high voltages. It illustrates processing opportunities for surface engineering and coating by high-oxygen-activity passivation, selective chemical alloying and strain engineering using wet chemistry.

High-energy lithium-ion batteries rely on the high-voltage operation of oxide cathodes to gain extra capacity. For example, for $Li_{1-x}CoO_2$, elevating the upper cut-off voltage U^{up} from 4.2–4.3 V to 4.6 V (versus Li^+/Li) increases the discharge capacity from 140–160 mAh g^{-1} to 215–220 mAh g^{-1} (ref. 1). However, oxygen anions in the solid oxide would become thermodynamically unstable at high enough voltage U and want to leave as gas, as represented by the reaction: $O^{2-}(\text{oxide}) = O_2(\text{gas}) / 2 + 2e^-(U)$. Effectively, it leads to an equilibrium oxygen partial pressure $P^{eq}(O_2) = \exp(4e(U - U^0)/k_BT)$ [atm], which increases by 5.2-*million*-fold per every 0.1 V increase in U, at absolute temperature $T = 300$ K (k_B is the Boltzmann constant, and e is the elementary charge). Here U^0 is the thermodynamic oxygen evolution reaction (OER) potential of the oxide ($P^{eq}(O_2) = 1$ atm), drawing an analogy to the 1.23 V U^0_{OER} stability boundary of room-temperature water, while replacing the 'liquid oxide' H_2O by a solid oxide. Huggins pointed out this oxygen crisis for cathodes and raised concerns about battery safety[2] because the aforementioned O_2(gas) or allied oxygen radicals (peroxide O^{1-}, superoxide $O^{0.5-}$) can react with the organic electrolyte, resulting in degradations and thermal runaways[3,4]. Huggins estimated U^0 to be 2.91 V (versus Li^+/Li) and proposed it to be independent of cathode's crystal structure and chemical composition, leading to a seemingly absurd number of $P^{eq}(O_2) > 10^{50}$ atm at 4.6 V. However, we do not think U^0 could be as low as 2.91 V for common layered oxide cathodes such as LCO ($LiCoO_2$) and NMC ($LiNi_uMn_vCo_{1-u-v}O_2$).

Taking LCO as an example, based on the Li-Co-O ternary phase diagram computed by density functional theory (DFT) at materialsproject.

[1]College of Chemistry and Molecular Engineering, Peking University, Beijing, China. [2]Department of Nuclear Science and Engineering, Massachusetts Institute of Technology, Cambridge, MA, USA. [3]State Key Laboratory of New Ceramics and Fine Processing, School of Materials Science and Engineering, Tsinghua University, Beijing, China. [4]Shanghai Institute of Ceramics, Chinese Academy of Sciences, Shanghai, China. [5]School of Materials Science and Engineering, Tianjin University of Technology, Tianjin, China. [6]College of Chemistry and Chemical Engineering and College of Energy and School of Energy Research, Xiamen University, Xiamen, China. [7]Shanghai Institute of Microsystem and Information Technology, Chinese Academy of Sciences, Shanghai, China. [8]College of Chemistry, Zhengzhou University, Zhengzhou, China. [9]Department of Materials Science and Engineering, Massachusetts Institute of Technology, Cambridge, MA, USA. [10]These authors contributed equally: Mingzhi Cai, Yanhao Dong. ✉e-mail: liju@mit.edu; huangfq@pku.edu

org[5,6], a small amount of O_2(gas) released from $Li_{1-x}CoO_2$ ($0 < x < 1/2$) would drive the composition inside the $LiCoO_2$-$Li_{1/2}CoO_2$-Co_3O_4 tie-line triangle (Supplementary Fig. 1), which fixes all three chemical potentials μ_{Li}, μ_O and μ_{Co}. The reaction $6Li_{1/2}CoO_2 \rightarrow 3LiCoO_2 + Co_3O_4 + O_2$(gas) with $Co^{2+}/Co^{3+}/Co^{4+}$ transition metal redox has a computed enthalpy change $\Delta h(O_2) = 2.159$ eV O_2^{-1}. This allows us to obtain an equilibrium $P^{eq}(O_2) = \exp(-\Delta h(O_2)/k_BT + \Delta s(O_2)/k_B) = 2.8 \times 10^{-26}$ atm if inside the $LiCoO_2$-$Li_{1/2}CoO_2$-Co_3O_4 tie-line triangle, based on the experimental gaseous O_2 entropy $\Delta s(O_2) = 205.3$ J mol$(O_2)^{-1}$ K^{-1} at the $P(O_2) = 1$ atm, $T = 300$ K reference state from the Joint Army Navy Air Force thermochemical table[5–7], when $x \rightarrow 0^+$ (beginning of charge) for $Li_{1-x}CoO_2$ at $U(x = 0^+) = 3.7$ V. On the basis of this, we predict $P^{eq}(O_2)$ would rise from 2.8×10^{-26} atm to 1 atm if at 0.38 V above $U(x = 0^+)$, namely $U^0 \approx 4.1$ V. By this reasoning, LCO can 'boil off' or evolve O_2(gas) bubbles at $U > 4.1$ V versus Li^+/Li, if not for the surface kinetic inhibitions for OER.

Even if $U < U^0$ and $P^{eq}(O_2)$ is less than 1 atm, say, 10^{-4} atm, because the organic electrolyte is chemically reactive, the cathode could still lose oxygen thermodynamically to the electrolyte and contaminate the latter. High U-driven decomposition of battery cathode should not be surprising and high-voltage cycling often triggers a series of detrimental processes, including surface composition change and phase transformation, transition metal (TM) dissolution and over-growth of cathode electrolyte interphases (CEIs)[8–11], which may all be attributed to the high $P^{eq}(O_2)$ driving force. It results in fast impedance growth, accelerated degradation and premature battery failure[12].

While we concur with the thermodynamic trend pointed out by Huggins, we consider further the following two aspects. First, we disagree that high-U cathodes are necessarily unsafe, because the 'surface' overpotential $\eta \equiv U - U^{eq}$ for OER due to Butler–Volmer charge transfer and other kinetic processes can run as large as 1 V to 2 V for H_2O OER[13]. Through material engineering, we should be able to utilize the high-U cathode capacity by resorting to large η_{OER} on the order of 1 V to 2 V. This is the name of the game, as the oxygen 'boiling' crisis at ~0.7 V above its initial $x = 0^+$ TM redox voltage is generic and not limited to LCO, but for all NMC, Li-rich, high-voltage spinel and disordered rock salt cathodes[9,10,14,15]. Secondly, it has been suggested[2] that poor electronic conductivity, but good ionic conductivities, on the surface passivation film is the reason for enlarged η_{OER}.

We believe quite differently and will demonstrate the opposite in our work. By creating a perovskite surface layer that has *high* electronic conductivity but *low* oxygen ion conductivity, we show the epitaxial nanolayer can act as an oxygen *buffer* that sustains large $\Delta P^{eq}(O_2)$ across, leading to an excellent kinetic inhibition of OER, while being highly transparent to both e^- and Li^+ to allow the proper functioning of the cathode. Thus, high electronic conductivity and a very low *oxygen* anion conductivity appear to be the key to large η_{OER} and a high binding energy of oxygen to the far right on the Sabatier 'volcano' plot to greatly decrease electrocatalytic (Butler–Volmer) surface activity for OER. Despite using the same perovskite structure, this materials design is actually opposite in purpose from the perovskite electrodes that *catalyse* OER in electrolyser cells[8,9,16].

Design criteria for ideal cathode surface architecture

We first outline the general design criteria (Fig. 1a) of the near-surface phase for high-voltage cathodes, especially those with hybrid anion- and cation-redox activities[17]. *Criterion a*: it should be non-active in terms of Li charging (delithiation). This avoids the formation of a massive amount of lithium vacancies and ensures phonon/lattice stability in the surface phase. *Criterion b*: it should be able to kinetically shut off oxygen motion and forbid the highly oxidizing oxygen radicals from touching the organic electrolytes. *Criterion c*: it needs to be a good mixed ionic (Li^+) and electronic conductor. *Criterion d*: it should be a poor OER catalyst. Instead of following the Sabatier principle for intermediate reactant–catalyst adsorption energy (that is, fine tuning to reach the top of the volcano plot) for rapid oxygen electrocatalysis[18], here we seek strongly bonded oxygen on the surface (that is, targeting for the very high binding energy side of the volcano plot). *Criterion e*: to fundamentally address the oxygen-loss issues in the highly delithiated cathode near the surface, it would be desirable to 'store' and encapsulate labile oxygen species in the near-surface phase so that oxygen transport is shut off. In other words, the surface phase should allow for a self-terminating 'oxygen buffering' process so that complete passivation of the high-oxygen-activity charged cathode to the electrolytes is achieved. In the literature, *Criteria a–c* are widely practiced; *Criterion d* points to covalent bonding or strong TM *d*-oxygen 2*p* hybridization such as polyanion and spinel cathodes[19–21], well known in the bulk cathode chemistry and recently practiced at the surface[22]; *Criterion e* is new and shall be demonstrated.

Our approach engineers the near-surface structure and creates a three-dimensionally connected perovskite structure surface phase satisfying the above criteria. For LCO, we first ion exchanged Li^+ near the surface with La^{3+} (major exchange cation) and Ca^{2+} (minor exchange cation) in an aqueous solution to form an implanted La/Ca gradient (Fig. 1b). Here the liquid solution completely wets the solid LCO particles, and the 'slow' ion-exchange process under ambient conditions offers uniform and tunable implantation. Upon annealing, the near-surface lattice would reconstruct into a Li-poor perovskite structure protection shell (Region I in Fig. 1c) and a La/Ca gradient-doped layered-structure buffer layer (Region II), which are epitaxial to both the bulk LCO (Region III) and the as-constructed surface phase (Region I). Meanwhile, the annealing temperature is kept low enough to freeze long-range La/Ca bulk diffusion and avoid chemical homogenization. Our approach is analogous to carburizing of steel surface[23]—carbon-rich atmosphere 'wets' the surface of the steel, carbon lattice-diffuses into the bulk and follow-up heating-and-quenching treatment phase-transforms the carbon-rich outer surface—thus termed 'lanthurization'.

Lanthurized surface architecture

We synthesized pristine LCO (P-LCO) via a solid-state method (X-ray diffraction, XRD in Supplementary Fig. 2 and scanning electron microscopy, SEM in Supplementary Fig. 3a). After Li^+-La^{3+}/Ca^{2+} ion exchange (confirmed by inductively coupled plasma-optical emission spectrometry, ICP-OES in Supplementary Table 1), we found a surface layer (~3 nm) with a different lattice spacing from the bulk LCO (Fig. 2a) and the incorporation of high-atomic-number elements (La and Ca) in the Li layer (Fig. 2b). The La/Ca incorporation is graded with a higher concentration at the surface, controlled by La^{3+}/Ca^{2+} lattice diffusion in the Li layer. X-ray photoelectron spectroscopy (XPS) in Fig. 2c shows La^{3+} and Ca^{2+} at ion-exchanged LCO surface.

The ion-exchanged LCO was heat treated to obtain lanthurized LCO (La-LCO), which has similar XRD (Supplementary Fig. 2) and morphology (Supplementary Fig. 3b) to P-LCO. (The heat-treatment temperature must be high enough for surface perovskite formation and not too high to activate long-range La/Ca diffusion in LCO lattice. Detailed rationale in Supplementary Fig. 4.) It creates a surface architecture schematically shown in Fig. 1c. Under STEM-HAADF (Fig. 2d,e), a high-symmetry surface structure (Region I, ~3 nm thick) was observed, whose fast Fourier transform (FFT) pattern (Fig. 2f) matches with a perovskite structure oxide $La_{1-w}Ca_wCoO_{3-\delta}$. Approximately 8% compressive strain was noted by comparing the lattice spacing ($d_{110} = 2.50$ Å and $d_{104} = 2.48$ Å) in real (Fig. 2e) and reciprocal spaces of Region I (Fig. 2f) with the reference ($d_{110} = 2.714$ Å and $d_{104} = 2.698$ Å). Oxygen vacancies in $La_{1-w}Ca_wCoO_{3-\delta}$ were observed by electron paramagnetic resonance (EPR, Supplementary Fig. 5)[24]. Between Region I and the bulk (Region III in Fig. 2d, whose lattice structure in Fig. 2g and FFT pattern in Fig. 2h match with $LiCoO_2$), a layered-structure buffer layer (Region II) with minor graded La/Ca doping (Fig. 2d and Supplementary Fig. 6) was observed. The surface architecture is confirmed by the line scan intensity

https://doi.org/10.1038/s41560-022-01179-3

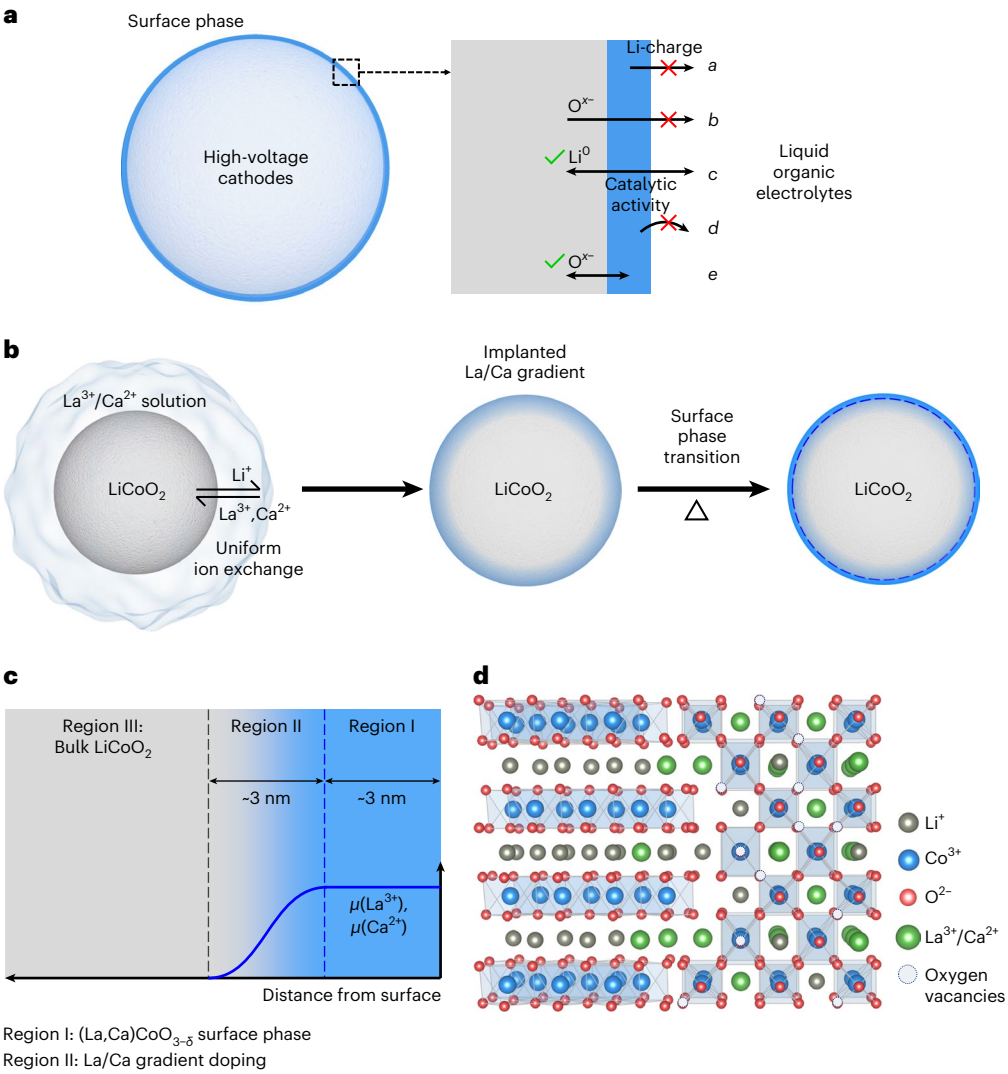

Fig. 1 | Design criteria of ideal surface coating and our solution. a, The ideal surface phase should satisfy the following design criteria: *a*, Li-charging inactive; *b*, kinetically shut-off oxygen ($O^{\alpha-}$, $0 \le \alpha \le 2$) outgassing from cathode to organic electrolytes; *c*, a good mixed ionic and electronic conductor to facilitate ambipolar Li diffusion; *d*, catalytically inactive and with strongly bonded surface oxygen; *e*, be able to encapsulate labile oxygen given out by highly delithiated cathode. **b**,**c**, Schematic lanthurizing treatment process (**b**) and obtained surface architecture and schematic chemical potential profile μ of La^{3+} and Ca^{2+} (**c**). δ denotes the oxygen off-stoichiometry. **d**, Schematic atomic structure of the surface architecture.

profile (Fig. 2i) along the Li layer of LCO. Remarkably, regions I–III are epitaxially bonded together, resulting in a gradient-strained layered structure in Region II and a compressively strained perovskite (~9 GPa built-in compressive stress estimated using 112 GPa modulus for $La_{1-w}Ca_wCoO_{3-\delta}$ (ref. 25)) in Region I and serving as a proof for high-quality conformal surface reconstruction.

For surface chemistry, Fig. 3b shows electron energy loss spectroscopy (EELS) spectra of La M-edge near La-LCO surface (Fig. 3a). The signal is the strongest at the surface and gradually diminishes in more bulk-like regions. For Co L-edge (Fig. 3c), a slight shift to higher EELS energy loss was observed at the surface, which is attributed to mixed Co^{3+} (major)/Co^{4+} (minor) valence in $La_{1-w}Ca_wCoO_{3-\delta}$ surface phase. Another interesting feature was observed in O K-edge (Fig. 3d), where the pre-edge peak at ~530 eV shifts to higher EELS energy loss and suggests stronger O bonds with neighbouring cations. To gain better statistics, Ar^+ sputtering-assisted XPS was measured on La-LCO powders. The La and Ca concentration gradients can be clearly seen in Fig. 3e,f (quantifications in Fig. 3g). O 1*s* spectra (Fig. 3h) also show obvious shifts to higher binding energy at the surface. The total amounts of incorporated La and Ca were quantified by ICP-OES (Supplementary Table 2), corresponding to 0.234 mol% La and 0.072 mol% Ca per mole LCO. Assuming +3 valence for Co, the composition of the surface perovskite is estimated to be $La_{0.76}Ca_{0.24}CoO_{2.88}$.

Electrochemical performance

When cycled at 3.0–4.5 V (versus Li^+/Li) in half cells, La-LCO has 185 mAh g^{-1} discharge capacity at 0.2 C (1 C = 200 mA g^{-1}) and 97.9% capacity retention over 600 cycles at 1 C (Fig. 4a, much better than P-LCO's 80% retention after 150 cycles). When U^{up} increases to 4.6 V, the discharge capacity of La-LCO increases to 210 mAh g^{-1} at 0.2 C, and 79.8% capacity retention is demonstrated over 500 cycles at 1 C (Fig. 4b versus faster decay of P-LCO; their charge–discharge curves at different cycles in Supplementary Fig. 7). Compared with P-LCO, La-LCO shows better rate performance (Fig. 4c) up to 10 C. We found the improved electrochemical performance is due to suppressed impedance growth (electrochemical impedance spectroscopy, EIS data in Supplementary Fig. 8 and Supplementary Table 3) and less overpotential build-up (galvanostatic intermittent titration technique,

https://doi.org/10.1038/s41560-022-01179-3

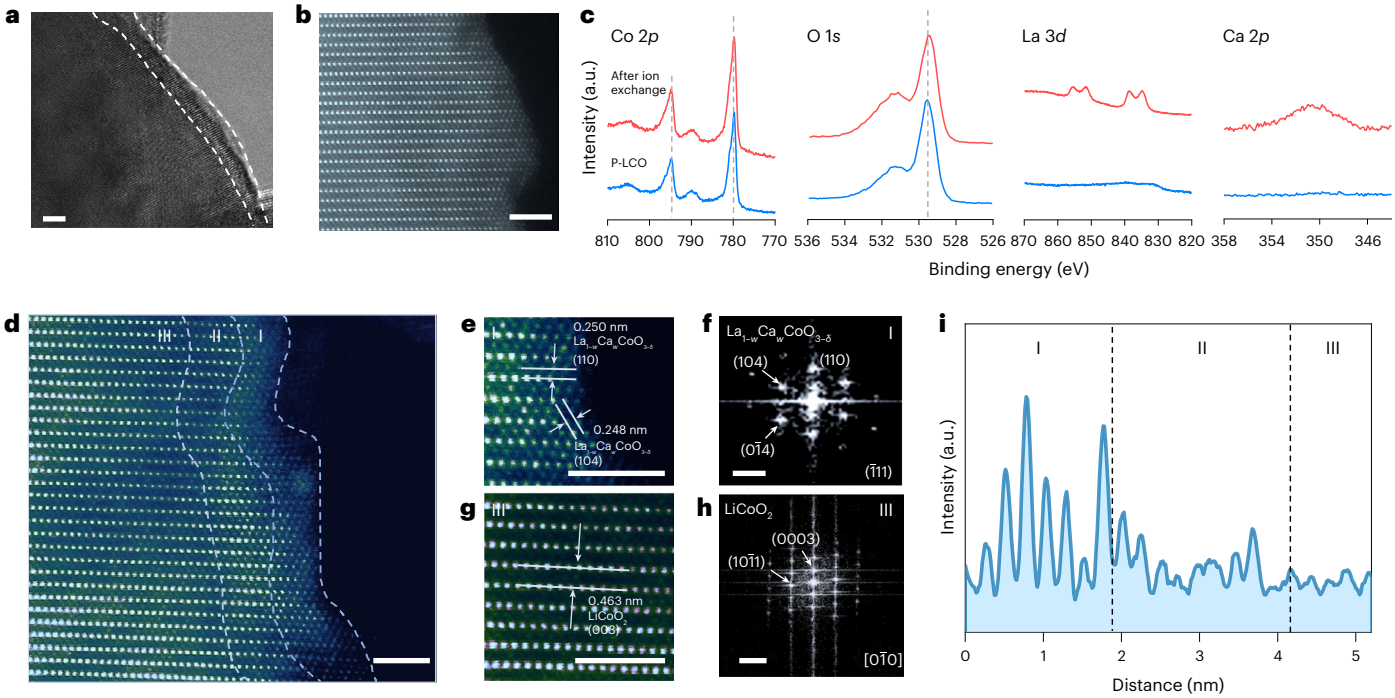

Fig. 2 | Surface architecture of lanthurized LCO. a–**c**, High-resolution transmission electron microscopy, HRTEM (**a**), scanning transmission electron microscopy under high-angle annular dark-field mode, STEM-HAADF (**b**), and XPS patterns of Co 2*p*, O 1*s*, La 3*d* and Ca 2*p* (**c**) of $LiCoO_2$ surface after ion exchange and before heat treatment. The vertical dashed lines are for guidance of eyes. Surface layer in **a** identified by lattice mismatch with the bulk LCO. **d**, HAADF-STEM of La-LCO surface (after heat treatment) showing an architecture consisting of Region I, II and III, separated by the dashed lines. **e**, HAADF-STEM of Region I. **f**, FFT pattern of **e** matching perovskite $La_{1-w}Ca_wCoO_{3-\delta}$ ($a = b = 5.434$ Å, $c = 13.076$ Å, $\alpha = \beta = 90°$, $\gamma = 120°$; with a rhombohedral structure that deviates from an ideal cubic perovskite structure). **g**, HAADF-STEM of Region III. **h**, FFT pattern of **g**. **i**, The intensity profile of the line scan along a Li layer of LCO (surface denoted as distance equal to zero). Scale bars, 2 nm (**a**,**b**,**d**,**e**,**g**), 5 nm^{-1} (**f**,**h**).

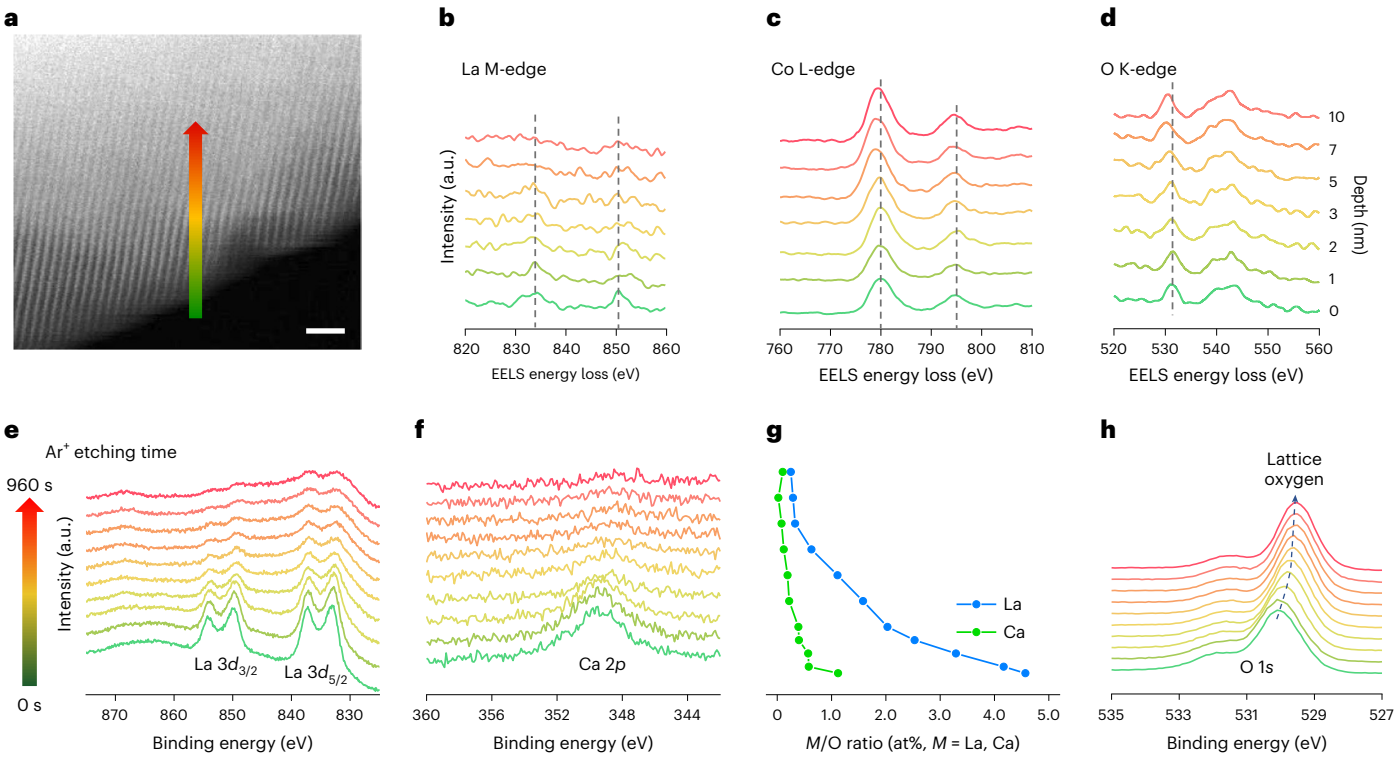

Fig. 3 | Gradient elements distribution at near surface of lanthurized LCO. a–**d**, STEM (**a**) of La-LCO surface with a colour-gradient arrow for EELS line profiling of La M-edge (**b**), Co L-edge (**c**) and O K-edge (**d**) at different depths. The vertical dashed lines are for guidance of eyes. **e**–**h**, XPS depth profiles of La 3*d* (**e**), Ca 2*p* (**f**), O 1*s* (**h**) of La-LCO and the corresponding quantity variation profile of La and Ca (**g**) as a function of Ar^+ etching time from 0 s to 960 s. Scale bar, 2 nm (**a**).

https://doi.org/10.1038/s41560-022-01179-3

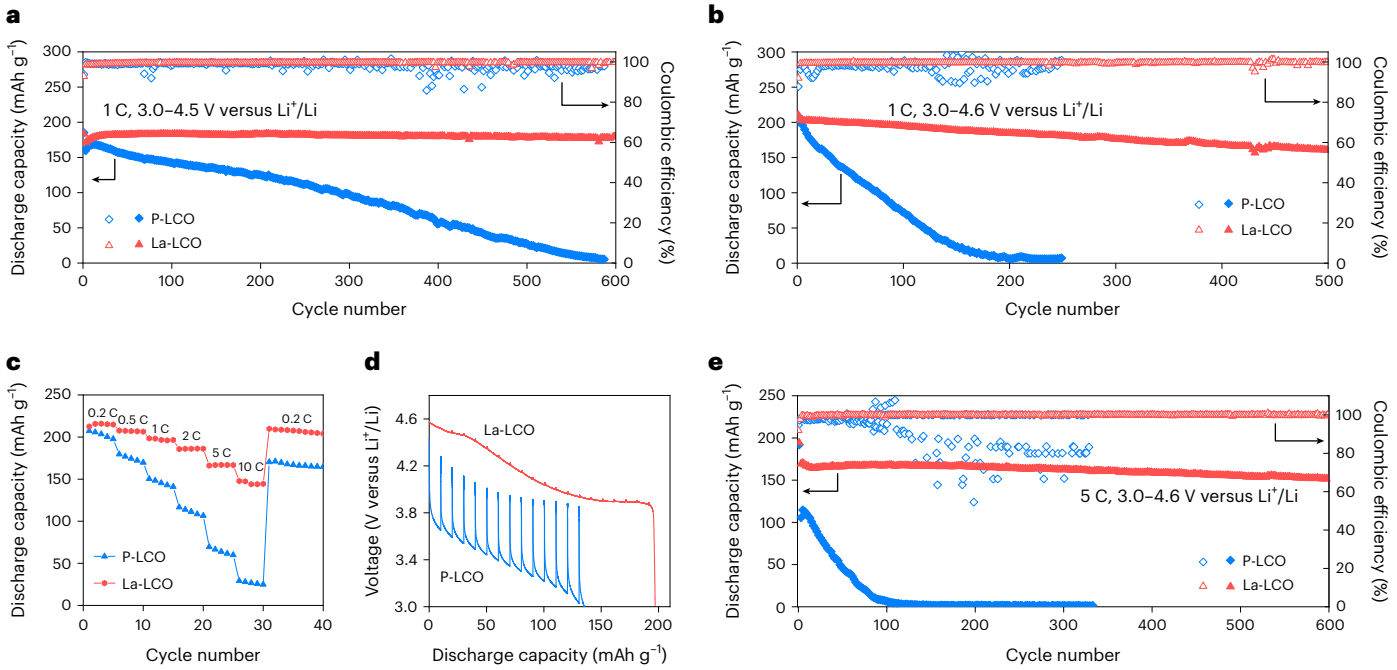

Fig. 4 | Superior electrochemical performance of La-LCO over P-LCO. a,**b**, 1 C cycling of La-LCO and P-LCO in coin-type half cells at 3.0–4.5 V (**a**) and 3.0–4.6 V (**b**) versus Li^+/Li. **c**, Rate performance of La-LCO and P-LCO at 3.0–4.6 V versus Li^+/Li. **d**, Discharge curves of GITT measurements (performed at 0.2 C) of La-LCO and P-LCO collected after 50 cycles at 1 C and 3.0–4.6 V versus Li^+/Li. **e**, 5 C/5 C charge/discharge cycling of La-LCO and P-LCO in coin-type half cells.

GITT data in Fig. 4d and calculated voltage losses data in Supplementary Fig. 9). The average discharge overpotential over the different states of charge is 0.024 ± 0.004 V (mean and standard deviation) for La-LCO after 50 cycles at 1 C, which is much smaller than that of P-LCO (1.064 ± 0.145 V). We further challenged the 4.6 V stability of La-LCO by conducting 5 C/5 C charge/discharge cycling. La-LCO can stably deliver 170 mAh g^{-1} discharge capacity and 89.4% capacity retention after 600 cycles (Fig. 4e), while P-LCO rapidly fails in <100 cycles. Lastly, we confirmed that the improvement comes from lanthurization rather than just the water treatment (Supplementary Fig. 10).

To evaluate the electrochemical performance of La-LCO under more practical conditions, we scaled up the synthesis to ~200 g per batch and assembled ~340 mAh (at 0.6 C) pouch-type full cells against graphite anode with high cathode loading (14.5 mg cm^{-2} per side, double side coated with 94 wt% active materials), high areal capacity (~2.8 mAh cm^{-2} per side at 0.6 C), and limited electrolytes (~3.5 g Ah^{-1}). When cycled at a full-cell voltage range between 3.0 V and 4.5 V (against graphite), the pouch cell with La-LCO cathode demonstrates excellent cycling stability at 200 mA/200 mA charge/discharge current (~0.6 C), with 84.4% capacity retention over 500 cycles (Fig. 5a), high average Coulombic efficiency (99.8%), stable charge–discharge curves (Fig. 5b), stable average discharge voltage (3.93 V, Fig. 5c) and high energy efficiency (~98%, Fig. 5d). The performance matrix is superior to the pouch cell with P-LCO cathode, which rapidly fails in less than 200 cycles. Elevating the upper cut-off voltage to 4.55 V further increases the full-cell energy (Supplementary Fig. 11). La-LCO again shows superior cycling stability than P-LCO in terms of discharge capacity, average discharge voltage and energy efficiency (Supplementary Fig. 12).

Oxygen-storage perovskite mitigates oxygen crisis

The constructed surface architecture stabilizes surface oxygen and suppresses gassing—thus mitigating the oxygen evolution crisis. Using in situ differential electrochemical mass spectrometry (DEMS), we found severe O_2 (onsets at ~4.33 V versus Li^+/Li) and CO_2 (onsets at ~4.17 V) gassing when first charging P-LCO (Fig. 6a), while it is much delayed for La-LCO (Fig. 6b; no O_2 gassing up to 4.7 V and CO_2 gassing onsets at ~4.57 V). (The accumulative O_2 emission decreased to approximately zero within the detection limit and the accumulative CO_2 emission decreased by 15.4 times.) Because O_2 and CO_2 evolution come from surface phase transformation (due to labile surface oxygen and often accompanied by TM reduction and dissolution) and oxidization of the organic electrolytes[9,17], our results indicate better surface passivation and stabilized surface oxygen. Equivalently, it represents increases in η_{OER} of 0.37 V and oxidation overpotential of 0.40 V in carbonate electrolyte. To further prove this, we measured the H_2O OER activity of P-LCO and La-LCO in 0.1 M KOH aqueous solution (Supplementary Fig. 13), where La-LCO indeed shows suppressed activity and larger η_{OER}.

The mitigated gassing is shown with the cycled pouch cells: the pouch cell using P-LCO has a significant volume expansion after 100 cycles (Fig. 6c), while the one using La-LCO remains the original dimensions (Fig. 6d). By comparing cryo-EPR spectra on uncharged, 4.3 V-charged, and 4.6 V-charged P-LCO (Fig. 6e), we found that significantly more oxygen vacancies[26,27] upon high-voltage charging (left behind by outgassing oxygen, reflecting damages from the oxygen crisis). In comparison, the amounts of oxygen vacancies in 4.3 V-charged and 4.6 V-charged La-LCO remain the same as in the uncharged state (all from non-stoichiometric surface perovskite).

A direct benefit from stabilized surface oxygen is the realization of stable surface Co^{4+}/Co^{3+} redox (oxygen loss would cause TM reduction at the surface). Figure 6f shows the oxidization of Co^{3+} to Co^{4+} at the surface of La-LCO upon charging to 4.6 V, while partial reduction of Co^{3+} to Co^{2+} was observed at P-LCO surface due to oxygen loss and surface phase transformation.

For atomistic understandings, we compared the projected density of states of O 2*p* states[22,28] in LCO, $LaCoO_3$ and strained $LaCoO_3$. We found −8% strain modifies the electronic structure of $LaCoO_3$ (Supplementary Fig. 14) and effectively lowers the energy of O 2*p* states (Fig. 6g–i). It results from stronger Co 3*d*–O 2*p* hybridizations in −8% strained $LaCoO_3$, which lowers the average energy of the O 2*p* states

https://doi.org/10.1038/s41560-022-01179-3

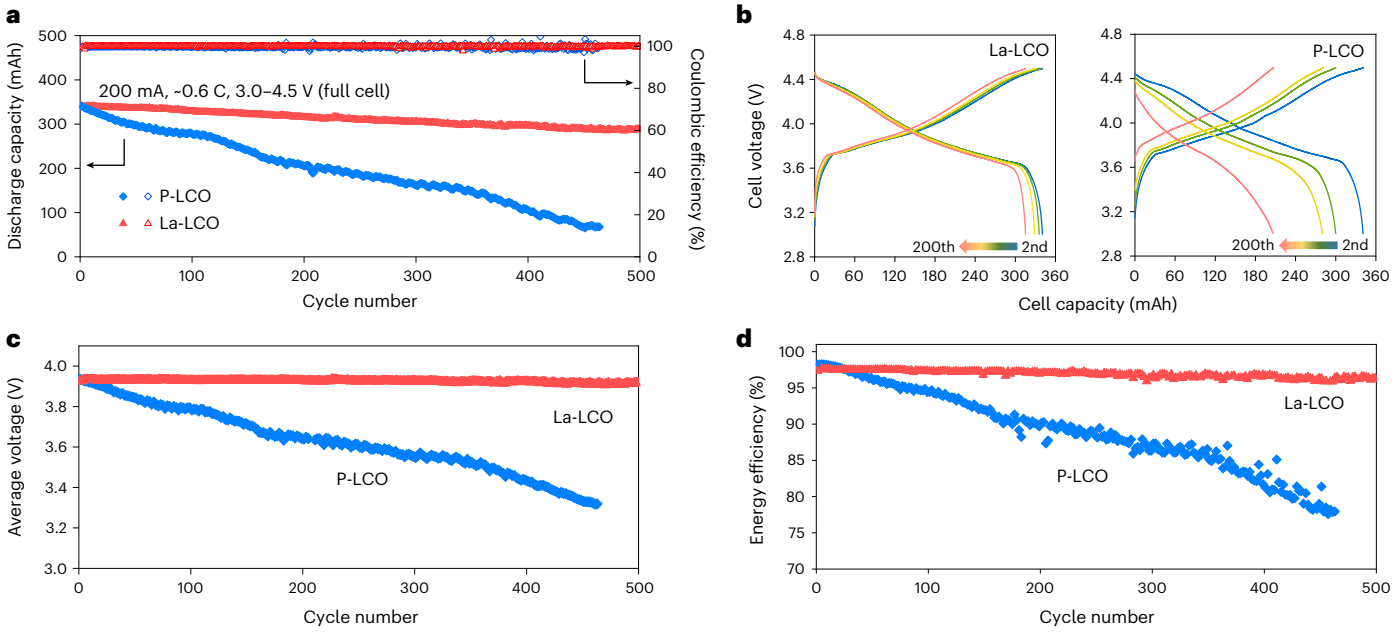

Fig. 5 | Full-cell performance of La-LCO and P-LCO. a, 200 mA (~0.6 C) cycling of La-LCO and P-LCO in pouch-type full cells against graphite anode at 3.0–4.5 V (full-cell voltage). **b**–**d**, Charge–discharge profiles at the second, 50th, 100th and 200th cycles (**b**), average discharge voltage (**c**) and energy efficiency (**d**) of La-LCO and P-LCO full cells in **b**.

from −2.7 eV (versus Fermi level E_F) in LCO and −2.8 eV (versus E_F) in $LaCoO_3$ to −4.4 eV (versus E_F) in −8% strained $LaCoO_3$. Such characteristics indicate better anodic stability (electron removal or hole filling) and strongly bonded oxygen. It suggests the strengthened oxygen–cation bonding is from compressive straining rather than the crystal structure. Indeed, in Supplementary Fig. 13, we found the powder form $La_{0.8}Ca_{0.2}CoO_{3-\delta}$ without epitaxial strain has similar OER activity as P-LCO, that is much higher than La-LCO.

Fine EELS measurements were next conducted on differently charged La-LCO particles (Fig. 6j), with 1 nm scanning interval and ~0.25 nm beam size. In uncharged state, we found a constant Co L_3/L_2 area ratio (which is used to analyse TM valence state; a lower ratio indicates oxidation or stronger TM–O bonds) around 2.61 at 5–20 nm from the surface, corresponding to Co^{3+} in bulk LCO. From 5 nm to 0 nm, Co L_3/L_2 area ratio gradually decreases, indicating strong Co–O bonds in the perovskite surface phase. When charged to 4.3 V, Co L_3/L_2 area ratio decreases due to Co oxidation. A constant value of 2.52 was noted for 7–20 nm from uniform delithiation of the bulk composition to $Li_{0.39}CoO_2$. For 0–7 nm, the ratio is again lower than the bulk, yet interestingly, the ratio at 0 nm does not change much. When further charged to 4.6 V, the ratio in the bulk (7–20 nm) decreases to around 2.40, and a striking surface profile is now resolved. We observed an obvious lowering in Co L_3/L_2 area ratio in Region I and a non-monotonic profile with a minimum at 4 nm at the interface between Region I and II. Because Region I does not contain as much Li^+ as bulk LCO does (some A-site Li^+ doping in perovskite is possible), the changes in Co L_3/L_2 area ratio in Region I should be contributed by other ions. We believe this is a strong indication for 'oxygen charging', namely, short-range migration of oxygen ions in highly delithiated LCO can fill in the oxygen vacancy in the perovskite structure, resulting in Co oxidation in Region I. The fact that the minimum Co L_3/L_2 area ratio shows up at the Region I/II interface further suggests maximum 'oxygen charging capacity' at the interface (that is, oxygen pile up). We argue that the perovskite surface phase 'stores' the outgassing oxygen species and encapsulates them from reacting with the electrolytes. Interestingly, when discharged to 3.0 V, the profile of Co L_3/L_2 area ratio returns to the original under the uncharged state. It means that the 'oxygen charging' process is reversible and the stored oxygen species in the perovskite surface phase can be given out and heal the bulk.

The benefit of the above process could be multi-fold: (1) lowering the energy of highly delithiated LCO lattice, (2) storing labile oxygen ions in the surface phase and suppressing the outgassing of oxygen species, (3) strengthening the anion sublattice of the surface phase so that the out-migration of oxygen species is self-terminated. Such an oxygen-storage surface phase verifies the *Design Criterion e* and is also the key to enhancing high-voltage cycling stability. Lastly, as a control sample, we conducted similar EELS measurements on different charged P-LCO (Supplementary Fig. 15). While similar bulk oxidations (5–20 nm) were observed when charged to 4.3 V and 4.6 V (at 4.6 V, Co oxidation in bulk P-LCO is slightly less than in bulk La-LCO), the surface Co is reduced because of surface oxygen loss. When discharged to 3.0 V, the reduced surface Co cannot be rejuvenated, and repeated cycling would form a Co_3O_4-like surface phase that degrades the performance.

Discussion

It is clear from the above results that lanthurizing improves high-voltage cycling stability and demonstrates stable 4.6 V (versus Li^+/Li) cycling performances (Supplementary Table 4 and 5). This is attributed to the uniform ion-exchange process, which reconstructs the near-surface region and ensures full coverage. The outcome is a uniquely strained, high-quality surface architecture (Region I + II), which is Li-poor and does not contain many lithium vacancies upon charging the cathode (*Criterion a*). This minimizes the driving force for electrochemical reconstruction, and phase transition typically happens at cathode surface after charging[29]. Post-cycling analysis shows that the lanthurized surface effectively suppresses surface transformation and CEI growth (Extended Data Fig. 1 and detailed discussions in Supplementary Note 1). Our well-constructed surface architecture physically separates organic electrolytes from delithiated cathodes in the bulk and kinetically blocks the oxygen outgassing (*Criterion b*). Obviously, the perovskite surface phase (Region I) should also have much better ionic and electronic conductivities than the cation-densified phase, which gives minimum overpotential for ambipolar Li^+ and electron transport

https://doi.org/10.1038/s41560-022-01179-3

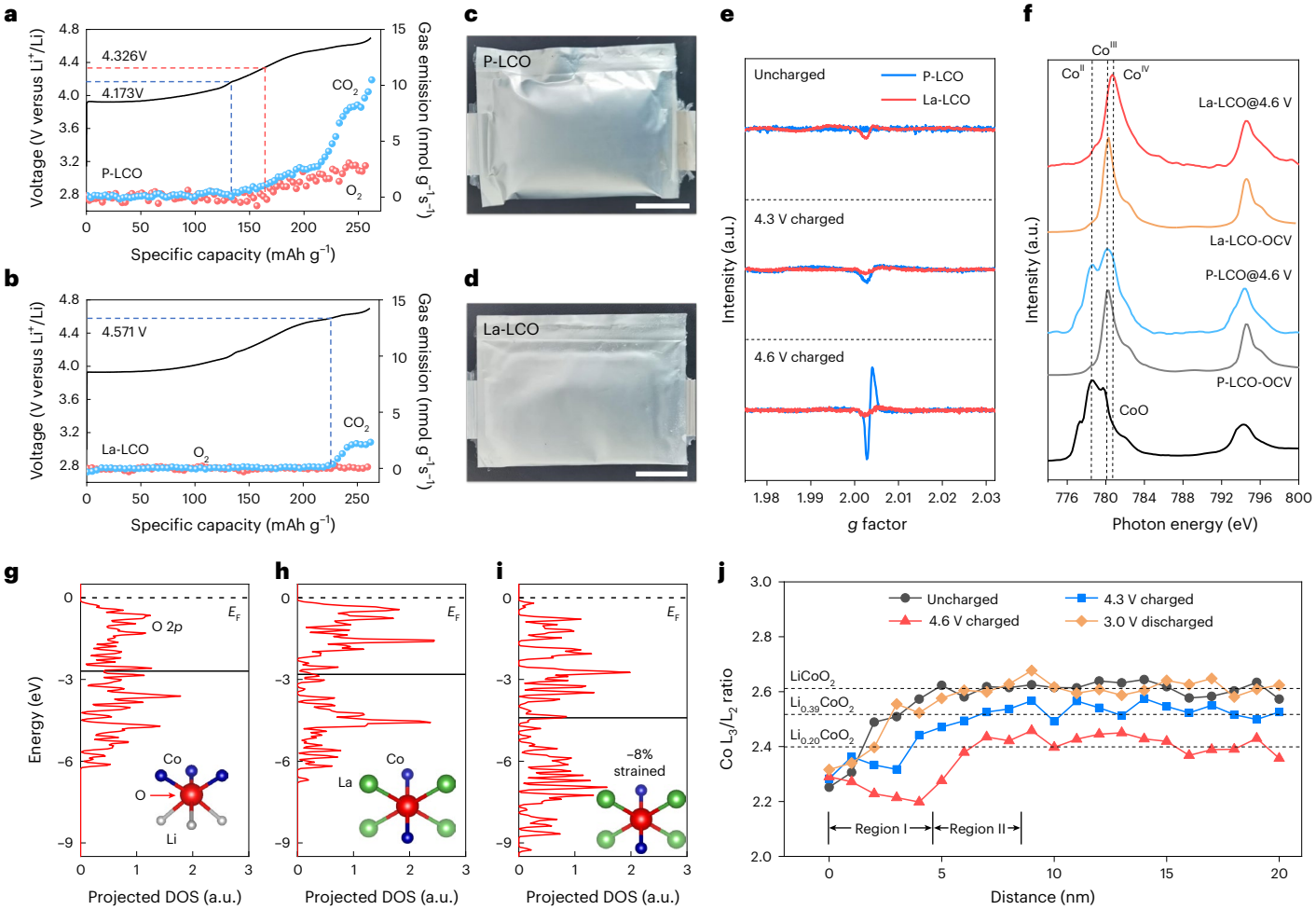

Fig. 6 | La-LCO with stabilized surface oxygen and oxygen storage surface phase. a,**b**, In situ DEMS profiles of P-LCO (**a**) and La-LCO (**b**) half cells performed during the first charge process to 4.7 V (versus Li^+/Li) at 0.1 C. **c**,**d**, Photos of P-LCO (**c**) and La-LCO (**d**) pouch cells after 100 cycles at 1 C and 3.0–4.5 V (full cell). Scale bars: 2 cm (**c**,**d**). **e**, EPR spectra of P-LCO and La-LCO under uncharged state and charged to 4.3 V and 4.6 V (versus Li^+/Li) at cryogenic temperature (90 K). **f**, sXAS under the mode of total electron yield (which is surface sensitive[40,41]) of Co L_2- and L_3-edges of P-LCO and La-LCO in uncharged and 4.6 V-charged states. (References for sXAS: CoO for Co^{2+}, P-LCO at OCV for Co^{3+} and literature reports[42,43] for Co^{4+}.) **g**–**i**, Projected density of states of O 2*p* states and the local schematic structures of oxygen (**g**–**i** insets) of LCO (**g**), unstrained $LaCoO_3$ (**h**) and −8% strained (minus sign denotes compressive strain) $LaCoO_3$ (**i**) from DFT calculations using Heyd–Scuseria–Ernzerhof exchange–correlation functional. E_F is the Fermi level. Solid lines in **g**–**i** denote the average energy of the O 2*p* states. **j**, Calculated Co L_3/L_2 area ratio for La-LCO under different charge states (uncharged, 4.3 V charged, 4.6 V charged and 3.0 V discharged). Dashed lines in **j** are referred Co states from the bulk (10–20 nm) for LCO (uncharged and 3.0 V-discharged), $Li_{0.39}CoO_2$ (4.3 V-charged) and $Li_{0.20}CoO_2$ (4.6 V-charged). For **j**, a sample with slightly thicker surface architecture, ~4–5 nm for Region I and ~4 nm for Region II, was characterized to better resolve the depth-dependent electrochemistry.

during charge/discharge. On the electronic part, we synthesized $La_{0.8}Ca_{0.2}CoO_{3-\delta}$ powders and measured the apparent electronic conductivity of the powder compacts of $La_{0.8}Ca_{0.2}CoO_{3-\delta}$, P-LCO, and La-LCO (Supplementary Table 6). We found $La_{0.8}Ca_{0.2}CoO_{3-\delta}$ has high electronic conductivity of 0.112 S cm^{-1}, which is 4,000 times higher than that of P-LCO (2.69×10^{-5} S cm^{-1}). Remarkably, despite the nanoscale surface modification, La-LCO has electronic conductivity of 2.75×10^{-4} S cm^{-1}, which is ten times higher than that of P-LCO. This should come from the highly conductive $La_{1-w}Ca_wCoO_{3-\delta}$ surface phase in La-LCO, which not only helps the particle-level conduction but also benefits long-range electron transport and electrode-level reaction homogeneity by removing kinetic bottlenecks[30]. On the ionic part, we assume some Li^+ cations doping on A sites readily exist in the $La_{1-w}Ca_wCoO_{3-\delta}$ phase (Region I), as supported by Supplementary Fig. 16, and some perovskites are known Li^+ conductors[31]. Therefore, we believe the nanoscale $La_{1-w}Ca_wCoO_{3-\delta}$ is a good mixed ionic and electronic conductor (*Criterion c*), which enhances rate capability. These characteristics, together with the strongly bonded surface oxygen (*Criterion d*) and the demonstrated oxygen-storage ability (*Criterion e*), demonstrate the perovskite surface phase as an example of the ideal coating materials.

In a broader context, Supplementary Note 2 shows that the lanthurization process can be readily applied to high-energy-density Co-lean/free cathodes such as Ni-rich $LiNi_{0.8}Co_{0.1}Mn_{0.1}O_2$ (NCM) and Li-/Mn-rich $Li_{1.2}Ni_{0.2}Mn_{0.6}O_2$ (LRNM). It improves the electrochemical performance of both NCM and LRNM (Extended Data Fig. 2), especially the high-voltage cycling stability up to 4.8 V (versus Li^+/Li). The surface perovskite has flexibility in the chemical space. From LCO to NCM and LRNM, the B-site cation could be Ni^{3+}, Co^{3+} and $Mn^{3+/4+}$. Following the selection strategy in Supplementary Note 3, we show that other lanthanide elements such as Pr^{3+}, Gd^{3+} and Yb^{3+} can be used as the major A-site cation in addition to La^{3+}. This leaves ample space for the design and optimization of such nanoscale surface perovskite.

Regarding the synthesis, Li^+–Na^+ ion exchange is known to produce interesting packing and novel cathodes[32,33]. To completely exchange the major cation Na^+ in the bulk, the Li^+–Na^+ exchange is typically conducted at elevated temperatures, in lithium molten salt, with excess

lithium salts and repeatedly. In comparison, our lanthurization seeks only to exchange surface Li^+ with minor La^{3+}/Ca^{2+}, thus can be conducted aqueously at ambient conditions and in a uniform, scalable manner. The lattice diffusivities of La^{3+} and Ca^{2+} are also much smaller than those of Li^+ and Na^+, which makes chemically graded surface architecture (epitaxially strained surface phase for Region I and gradient doping for Region II) possible.

Conclusions

To summarize, we have improved a theory of degradation-initiating oxygen crisis in high-energy-density layered cathodes and demonstrated a lanthurizing approach for stabilized high-voltage cycling. We showed that nanoscale $La_{1-w}Ca_wCoO_{3-\delta}$ surface phase can serve as an oxygen buffer and reversibly uptake oxygen ions, while impeding oxygen mobility and de-catalysing OER by ~0.4 V higher η_{OER}. In the oxidation of metals, a surface passivation layer can sustain a change in $P^{eq}(O_2)$ from 0.21 atm to an astronomically lower value such as 10^{-50} atm. We demonstrated the reverse, or 'pressure-vessel passivation oxide', that can sustain $\Delta P^{eq}(O_2) \approx 10^{47}$ atm across in the thermochemical sense. Our lanthurization approach widens the anodic stability window of oxide cathodes and suppresses surface side reactions, impedance growth and electrochemical degradation. The oxygen vacancy containing perovskite surface phase can store and encapsulate labile oxygen ions injected from near-surface delithiated cathode lattice. Beyond lithium-ion battery cathodes, our approach opens many opportunities in surface engineering of energy materials and elastic strain engineering[34] of nanometric oxide phases via scalable chemical routes.

Methods

Materials synthesis

P-LCO was synthesized via a solid-state method. Stoichiometric amounts of Co_3O_4 and Li_2CO_3 were mixed thoroughly in an agate mortar and heat treated at 950 °C for 10 h in air, with 5 wt% excess Li_2CO_3 added to compensate for high-temperature lithium loss. To synthesize La-LCO, an aqueous solution containing 0.4 M $LaCl_3$ and 0.4 M $CaCl_2$ was first prepared. Two g P-LCO was added to 5 ml as-prepared solution, followed by ultrasound dispersion, and then continuously stirred at room temperature for 24 h for ion exchange. The collected powders were washed using deionized water and dried at 80 °C for 12 h. The final La-LCO powders were obtained by heat treating the dried powders at 600 °C for 6 h in air. P-NCM and P-LRNM were synthesized by a co-precipitation method followed by a solid-state reaction with lithium salt. For P-NCM, $MnSO_4{\cdot}H_2O$, $CoSO_4{\cdot}7H_2O$ and $NiSO_4{\cdot}6H_2O$ were first dissolved in deionized water with 8:1:1 molar ratio and a total concentration of 2 mol l^{-1}. A mixture of 0.3 M $NH_3{\cdot}H_2O$ and 4 M NaOH were then added slowly at 50 °C under stirring, during which the pH value was controlled to 10.5–11.5 to obtain the hydroxide precursor. Then the hydroxide precursor was dried and mixed thoroughly with 3 wt% excess $LiOH{\cdot}H_2O$ in an agate mortar, followed by calcination at 500 °C for 2 h and 800 °C for 12 h in flowing oxygen to obtain P-NCM. For Co-free P-LRNM, 1.5 M $MnSO_4{\cdot}H_2O$ and 0.5 M $NiSO_4{\cdot}6H_2O$ were used as the TM solution, a mixed solution of 0.56 M NH_4HCO_3 and 2 M Na_2CO_3 was used as the precipitant to get the carbonate precursor $Ni_{0.25}Mn_{0.75}CO_3$. The reaction temperature was controlled to 50 °C and pH value was set to 7.8–8.1. The precursor was dried, mixed with 3 wt% excess Li_2CO_3 thoroughly and calcined at 600 °C for 4 h and 850 °C for 15 h to obtain P-LNRM. To synthesize La-NCM and La-LNRM, 0.4 M $LaCl_3$ and 0.4 M $CaCl_2$ mixed solution with DMF as solvent was first prepared. P-NCM and P-LRNM were then added, dispersed using ultrasound and violently stirred for 2 h at room temperature (for La-NCM) or 12 h at 50 °C (for La-LNRM). The collected powders were washed using DMF and dried at 80 °C for 12 h, followed by heat treatment at 720 °C in flowing oxygen (for La-NCM) or at 675 °C in air (for La-LNRM).

Materials characterizations

Powder XRD was conducted on a Bruker D2 X-ray diffractometer with Cu Kα radiation (λ = 1.5418 Å) with a scanning rate of 2° min^{-1} and within a 2θ range between 10° and 80°. SEM was conducted on an S4800 field emission scanning electron microscope. XPS was conducted on a spectrometer (Axis Ultra of Kratos Analytical Ltd.) with Al Kα radiation source ($h\nu$ = 1,486.7 eV) and depth profiles were obtained by assisted Ar^+ etching. Cycled samples were washed three times by dimethyl carbonate (DMC) to remove the residue electrolyte salts before XPS measurements. HRTEM was conducted on a field emission JEOL 2010F transmission electron microscope. STEM-HAADF, ABF, EDS mapping were conducted on an aberration-corrected FEI-Titan Cubed Themis G2 300 scanning transmission electron microscope operating at 300 kV. EELS were conducted on an aberration-corrected JEM-ARM300F scanning transmission electron microscope operating at 300 kV with a spatial resolution of 0.063 nm and energy resolution of 0.3 eV. For EELS measurements, a dual-EELS mode was applied. For EELS analysis, all the spectra were calibrated by zero-loss peak in the low-loss spectra, and a power-law background was used to extract the core loss signal. Peak shift and integral intensity ratio of Co L_3/L_2 peak were used to analyse the Co valence. All the samples inspected by STEM were thinned to less than 100 nm using a 2–30 kV Ga ion beam on a dual-bean Helios Nanolab 460HP FIB-SEM system. The evolution of CO_2 and O_2 gases in coin-type half cells was tested by in situ DEMS in a custom-made cell with a detecting hole on the cathode side. Elemental compositions were measured by ICP-OES (Prodigy 7, Leeman Ltd.). Synchrotron soft X-ray absorption spectroscopy (sXAS) measurements were conducted at beamline 02B02 of the SiP·ME2 platform at the Shanghai Synchrotron Radiation Facility. The bending magnet beamline provided photons with an energy range from 50 eV to 2,000 eV. The photon flux was ~10^{11} photons s^{-1} and the energy resolving power was up to 13,000. The beam sizes at the measured samples were set to 150 μm × 50 μm. L-edge of Co was collected using surface-sensitive total electron yield mode at room temperature in an ultrahigh vacuum chamber with a base pressure better than 1×10^{-9} Torr. EPR spectra were collected from powders or differently charged electrodes on a Bruker EMX PLUS spectrometer in 9.3 GHz at cryogenic temperature (90 K, to minimize noise and gain better sensitivity) with a power of 6.325 mW. The modulation amplitude was set to 3.000 G at a modulation frequency of 100.00 kHz. To eliminate the influence of conductive carbon, conductive carbon-free electrodes were used for EPR tests under different charge states (mass ratio of active materials to binder polyvinylidene fluoride, PVDF, was set as 9:1).

Electrochemical measurements

For coin-type half cells, cathode slurry was prepared by active materials, acetylene black and PVDF with a weight ratio of 8:1:1 (for LCO) or 90:5:5 (for NCM and LRNM) using N-methyl-2-pyrrolidone (NMP) as the solvent. The obtained slurry was coated onto an Al foil current collector and dried at 110 °C under vacuum for 10 h. The punched electrodes have a diameter of 14 mm and a cathode loading of 4–5 mg cm^{-2}. Half cells were assembled using 2016 R coin-type cells in an argon glovebox with H_2O and O_2 content below 0.1 ppm. Lithium metal foils of 1.6 mm-thickness (China Energy Lithium Co., Ltd.) with a diameter of 15 mm were used as the counter electrodes. 1 M $LiPF_6$ dissolved in a 1:1 (volume) ethylene carbonate (EC)/DMC mixture was used as the electrolyte for $LiCoO_2$ and Ni-rich cathodes, while 1 M $LiPF_6$ dissolved in a 1:1:1 (volume) EC/DMC/ethyl methyl carbonate (EMC) mixture with 5 wt% fluoroethylene carbonate (FEC) was used as the electrolyte for Li-rich cathodes. Glass fibre separator was used. For the first cycle (formation cycle), all coin cells were charged and discharged at 0.2 C (1.0 C defined as 200 mAh g^{-1}) and between the specified voltage range. Cycling stability and rate performance were next evaluated as specified in the main text. GITT measurements for LCO were conducted on half cells after the 3rd and 50th cycles at 1 C within 3.0–4.6 V (versus Li^+/Li)

with a titration current of 0.2 C, a titration time of 15 min and a relaxation time of 1 h. The above electrochemical measurements were conducted on a Neware battery test system (CT-4008Tn). EIS measurements were conducted on an automated electrochemical workstation (CHI660E). EIS was measured at a frequency range between 0.01 Hz and 10 MHz with zero direct current (d.c.) voltage and 5 mV alternating current (a.c.) amplitude.

Pouch-type full cells against graphite anode were prepared and assembled in a dry room with a dew point below −41 °C. Cathode slurry was prepared by 94 wt% active materials, 3 wt% acetylene black and 3 wt% PVDF using NMP as the solvent. The obtained cathode slurry was coated onto an Al foil current collector and dried at 120 °C for 24 h. Anode slurry was prepared by 94.5 wt% active materials (graphite anode), 2 wt% acetylene black, 1.5 wt% sodium carboxymethyl cellulose and 2 wt% styrene butadiene rubber using water as the solvent. The obtained anode slurry was coated onto a Cu foil current collector and dried at 120 °C for 24 h. The coating and drying processes were repeated to obtain double-sided coated electrodes. The cathode loading was controlled as 14.5 mg cm^{-2} (on each side of the Al foil current collector). The anode loading was controlled as 8.5 mg cm^{-2} (on each side of the Cu foil current collector). Commercial polyethylene film was used as the separator. 1 M $LiPF_6$ dissolved in a 1:1 (volume) EC/DMC mixture was used as the electrolyte. The electrolyte amount was controlled as ~3.5 g Ah^{-1}. The negative to positive capacity ratio (N/P ratio) was controlled as 1.10 ± 0.01. The assembled full cells were first cycled for two cycles to complete the formation process before the long-term cycling specified in the main text. The formation process is: the first charge cycle was conducted by charging the assembled cells at 0.2 C for 2 h and rested for 15 min, repeating this process twice, and then charging to 4.5 V or 4.55 V at 0.2 C; the first discharge cycle was conducted by discharging the cells to 3.0 V at 0.2 C; the second charge–discharge cycle was conducted at 0.2 C at 3.0–4.5 V or 3.0–4.55 V. All the electrochemical measurements of the full cells were conducted on a Land CT2001A battery test system.

To evaluate room-temperature OER activity in aqueous solutions, electrocatalytic measurements were performed in a three-electrode cell using a glassy carbon rotating disk electrode (diameter: 5 mm). Hg/HgO (1 M NaOH) was used as the reference electrode. Graphite rod was used as the counter electrode. 0.1 M KOH aqueous solution with continuous O_2 bubbling was used as the electrolyte. To prepare the testing materials loaded electrodes, 5 mg active materials (P-LCO, La-LCO or $La_{0.8}Ca_{0.2}CoO_{3-\delta}$ powders) and 1 mg carbon black were dispersed in 1 ml Nafion/alcohol solution (0.5 wt%) under ultrasound and stirred for 4 h to obtain a homogenous ink and 10 µl ink were coated on the glassy carbon electrode with a mass loading of 255 µg cm^{-2}. To remove gas bubbles formed at the surface of the active materials, the working electrode was rotated at 2,000 r.p.m. Linear sweep voltammetry was conducted at 10 mV s^{-1}.

Simulations

Spin-polarized DFT calculations using Heyd–Scuseria–Ernzerhof exchange–correlation functional were conducted by the Vienna ab initio simulations package[35–38]. The projector augmented wave potentials with a valence configuration of 1 electron for Li, 11 electrons for La, 9 electrons for Co and 6 electrons for O were used. A range-separation parameter of 0.2 in the range-separated hybrid functionals was used. The plane wave cut-off energy was chosen as 520 eV. The convergence criterion was chosen as residue atomic forces less than 0.01 eV $Å^{-1}$. Layered $LiCoO_2$ was simulated with a supercell containing 2 Li, 2 Co and 4 O, and the Brillouin zone was sampled using a Gamma scheme with 6 × 6 × 2 k-point mesh. Unstrained cubic $LaCoO_3$ was simulated with a supercell containing 1 La, 1 Co and 3 O by allowing the supercell size and shape to relax, and the Brillouin zone was sampled using a Gamma scheme with 5 × 5 × 5 k-point mesh. Strained cubic $LaCoO_3$ was simulated by applying −8% hydrostatic strain on the relaxed supercell of unstrained cubic $LaCoO_3$, and the Brillouin zone was sampled using a Gamma scheme with 5 × 5 × 5 k-point mesh. The atomic structures were plotted using VESTA[39].

Data availability

Data supporting the findings in the present work are available in the manuscript and supplementary information.

References

1. Yang, Q. et al. Surface-protected $LiCoO_2$ with ultrathin solid oxide electrolyte film for high-voltage lithium ion batteries and lithium polymer batteries. *J. Power Sources* **388**, 65–70 (2018).
2. Huggins, R. A. Do you really want an unsafe battery? *J. Electrochem. Soc.* **160**, A3001 (2013).
3. Sun, C. et al. High-voltage cycling induced thermal vulnerability in $LiCoO_2$ cathode: cation loss and oxygen release driven by oxygen vacancy migration. *ACS Nano* **14**, 6181–6190 (2020).
4. Hu, E. et al. Oxygen-redox reactions in $LiCoO_2$ cathode without O–O bonding during charge–discharge. *Joule* **5**, 720–736 (2021).
5. Ong, S. P., Wang, L., Kang, B. & Ceder, G. Li–Fe–P–O_2 phase diagram from first principles calculations. *Chem. Mater.* **20**, 1798–1807 (2008).
6. Ong, S. P., Jain, A., Hautier, G., Kang, B. & Ceder, G. Thermal stabilities of delithiated olivine MPO_4 (M=Fe, Mn) cathodes investigated using first principles calculations. *Electrochem. Commun.* **12**, 427–430 (2010).
7. Liu, M. et al. Spinel compounds as multivalent battery cathodes: a systematic evaluation based on ab initio calculations. *Energy Environ. Sci.* **8**, 964–974 (2015).
8. Li, J. et al. Structural origin of the high-voltage instability of lithium cobalt oxide. *Nat. Nanotechnol.* **16**, 599–605 (2021).
9. Zhu, Z. et al. Gradient Li-rich oxide cathode particles immunized against oxygen release by a molten salt treatment. *Nat. Energy* **4**, 1049–1058 (2019).
10. Zhang, S., Ma, J., Hu, Z., Cui, G. & Chen, L. Identifying and addressing critical challenges of high-voltage layered ternary oxide cathode materials. *Chem. Mater.* **31**, 6033–6065 (2019).
11. Zhang, F. et al. Surface regulation enables high stability of single-crystal lithium-ion cathodes at high voltage. *Nat. Commun.* **11**, 3050 (2020).
12. Dong, Y-H. & Li, J. Oxide cathodes: functions, instabilities, self healing, and degradation mitigations. *Chem. Rev.* (in the press).
13. Heard, D. M. & Lennox, A. J. Electrode materials in modern organic electrochemistry. *Angew. Chem. Int. Ed.* **59**, 18866–18884 (2020).
14. Zhao, E. et al. Structural and mechanistic revelations on high capacity cation-disordered Li-rich oxides for rechargeable Li-ion batteries. *Energy Storage Mater.* **16**, 354–363 (2019).
15. Liu, H. et al. Insight into the role of metal–oxygen bond and O 2*p* hole in high-voltage cathode $LiNi_xMn_{2-x}O_4$. *J. Phys. Chem. C.* **121**, 16079––16087 (2017).
16. Antipin, D. & Risch, M. Trends of epitaxial perovskite oxide films catalyzing the oxygen evolution reaction in alkaline media. *J. Phys. Energy* **2**, 032003 (2020).
17. Zhu, Z. et al. Gradient-morph $LiCoO_2$ single crystals with stabilized energy density above 3,400 W h L^{-1}. *Energy Environ. Sci.* **13**, 1865–1878 (2020).
18. Suntivich, J., May, K. J., Gasteiger, H. A., Goodenough, J. B. & Shao-Horn, Y. A perovskite oxide optimized for oxygen evolution catalysis from molecular orbital principles. *Science* **334**, 1383–1385 (2011).
19. Manthiram, A. & Goodenough, J. B. Lithium-based polyanion oxide cathodes. *Nat. Energy* **6**, 844–845 (2021).
20. Thackeray, M. & Amine, K. $LiMn_2O_4$ spinel and substituted cathodes. *Nat. Energy* **6**, 566–566 (2021).

21. Huang, Y. et al. Lithium manganese spinel cathodes for lithium-ion batteries. *Adv. Energy Mater.* **11**, 2000997 (2021).
22. Yoon, M. et al. Reactive boride infusion stabilizes Ni-rich cathodes for lithium-ion batteries. *Nat. Energy* **6**, 362–371 (2021).
23. Parrish, G. *Carburizing: Microstructures and Properties* (Asm International, 1999).
24. Zhou, M. et al. Enhancing the intrinsic activity and stability of perovskite cobaltite at elevated temperature through surface stress. *Small* **17**, 2104144 (2021).
25. Orlovskaya, N., Kleveland, K., Grande, T. & Einarsrud, M. A. Mechanical properties of $LaCoO_3$ based ceramics. *J. Eur. Ceram. Soc.* **20**, 51–56 (2000).
26. Wang, J. et al. Ultrathin $LiCoO_2$ nanosheets: an efficient water-oxidation catalyst. *ACS Appl. Mater. Inter.* **9**, 7100–7107 (2017).
27. Zhao, R. et al. The origin of heavy element doping to relieve the lattice thermal vibration of layered materials for high energy density Li ion cathodes. *J. Mater. Chem. A* **8**, 12424–12435 (2020).
28. Seo, D. H. et al. The structural and chemical origin of the oxygen redox activity in layered and cation-disordered Li-excess cathode materials. *Nat. Chem.* **8**, 692–697 (2016).
29. Yoon, M. et al. Unveiling nickel chemistry in stabilizing high-voltage cobalt-rich cathodes for lithium-ion batteries. *Adv. Funct. Mater.* **30**, 1907903 (2020).
30. Dong, Y. et al. Potential jumps at transport bottlenecks cause instability of nominally ionic solid electrolytes in electrochemical cells. *Acta Mater.* **199**, 264–277 (2020).
31. Inaguma, Y. et al. High ionic conductivity in lithium lanthanum titanate. *Solid State Commun.* **86**, 689–693 (1993).
32. Kang, K., Meng, Y., Breger, J., Grey, C. P. & Ceder, G. Electrodes with high power and high capacity for rechargeable lithium batteries. *Science* **311**, 977–980 (2006).
33. Cao, X. et al. Stabilizing anionic redox chemistry in a Mn-based layered oxide cathode constructed by Li-deficient pristine state. *Adv. Mater.* **33**, 2004280 (2021).
34. Li, J. EML webinar overview: elastic strain engineering for unprecedented properties. *Extreme Mech. Lett.* **54**, 101430 (2022).
35. Kresse, G. & Joubert, D. From ultrasoft pseudopotentials to the projector augmented-wave method. *Phys. Rev. B* **59**, 1758 (1999).
36. Kresse, G. & Furthmüller, J. Efficiency of ab-initio total energy calculations for metals and semiconductors using a plane-wave basis set. *Comput. Mater. Sci.* **6**, 15–50 (1996).
37. Perdew, J. P., Burke, K. & Ernzerhof, M. Generalized gradient approximation made simple. *Phys. Rev. Lett.* **77**, 3865–3868 (1996).
38. Krukau, A. V., Vydrov, O. A., Izmaylov, A. F. & Scuseria, G. E. Influence of the exchange screening parameter on the performance of screened hybrid functionals. *J. Chem. Phys.* **125**, 224106 (2006).
39. Momma, K. & Izumi, F. VESTA 3 for three-dimensional visualization of crystal, volumetric and morphology data. *J. Appl. Crystallogr.* **44**, 1272–1276 (2011).
40. Lin, F. et al. Synchrotron X-ray analytical techniques for studying materials electrochemistry in rechargeable batteries. *Chem. Rev.* **117**, 13123–13186 (2017).
41. Ren, G. et al. Photon-in/photon-out endstation for studies of energy materials at beamline 02B02 of Shanghai Synchrotron Radiation Facility. *Chin. Phys. B* **29**, 016101 (2020).
42. Yoon, W. S. et al. Oxygen contribution on Li-ion intercalation–deintercalation in $LiCoO_2$ investigated by O K-edge and Co L-edge X-ray absorption spectroscopy. *J. Phys. Chem. B* **106**, 2526–2532 (2002).
43. Zhao, J. et al. Electronic structure evolutions driven by oxygen vacancy in $SrCoO_{3-x}$ films. *Sci. China Mater.* **62**, 1162–1168 (2019).

Acknowledgements

F.H. acknowledges support by the National Natural Science Foundation of China (grants 21871008, 11227902), the Science and Technology Commission of Shanghai (grant 18YF1427200) and the Key Research Program of Frontier Science, Chinese Academy of Sciences (grant number QYZDJ-SSW-JSC013). J.L. acknowledges support from Samsung Advanced Institute of Technology. We thank beamline 02B02 of the Shanghai Synchrotron Radiation Facility for providing the beamtime.

Author contributions

F.H. conceived the project. J.L. developed the theory. M.C. and F.H. synthesized the materials and conducted the electrochemical measurements. Y.D. and H.X. conducted the simulations. M.C. and M.X. assembled and tested pouch-type full cells. P.D. conducted in situ DEMS measurements. H.Z. conducted sXAS measurements. S.Z. conducted XPS depth profile measurements. M.C., Y.D. and F.H. analysed the data. M.C., Y.D., J.L. and F.H. wrote the paper. All authors discussed and contributed to the writing.

Competing interests

The authors declare no competing interests.

Additional information

Extended data is available for this paper at https://doi.org/10.1038/s41560-022-01179-3.

Supplementary information The online version contains supplementary material available at https://doi.org/10.1038/s41560-022-01179-3.

Correspondence and requests for materials should be addressed to Ju Li or Fuqiang Huang.

Peer review information *Nature Energy* thanks the anonymous reviewers for their contribution to the peer review of this work.

Reprints and permissions information is available at www.nature.com/reprints.

Publisher's note Springer Nature remains neutral with regard to jurisdictional claims in published maps and institutional affiliations.

Springer Nature or its licensor (e.g. a society or other partner) holds exclusive rights to this article under a publishing agreement with the author(s) or other rightsholder(s); author self-archiving of the accepted manuscript version of this article is solely governed by the terms of such publishing agreement and applicable law.

© The Author(s), under exclusive licence to Springer Nature Limited 2023

https://doi.org/10.1038/s41560-022-01179-3

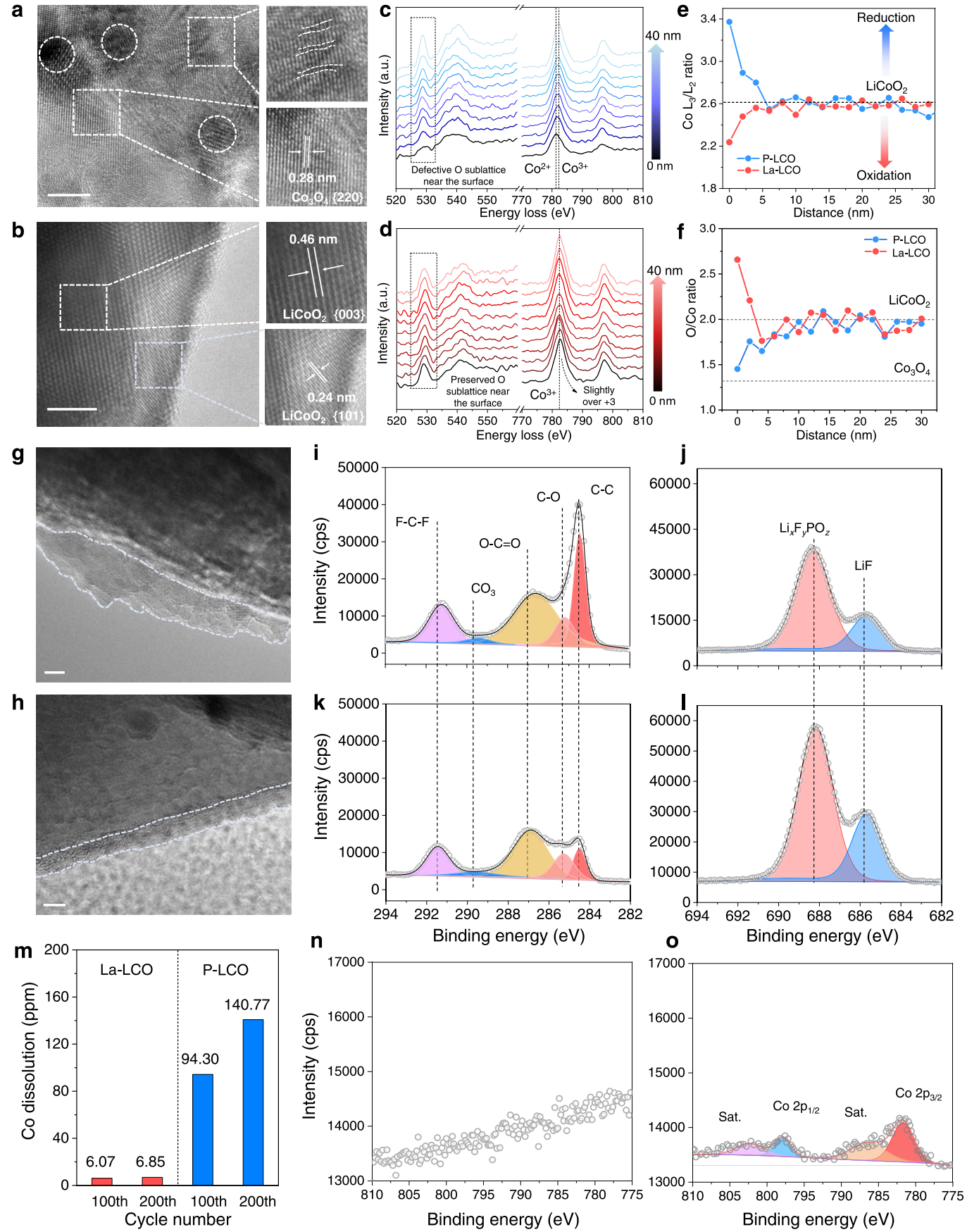

Extended Data Fig. 1 | See next page for caption.

https://doi.org/10.1038/s41560-022-01179-3

Extended Data Fig. 1 | Post-cycling morphological, structural and chemical characteristics of oxide surface and CEIs. a, **b**, HRTEM near the surface of cycled P-LCO (**a**) and La-LCO (**b**). Circled in (**a**) are Moire effects produced by lattice distortion. **c**, **d**, Depth-resolved EELS profiles near the surface of cycled P-LCO (**c**) and La-LCO (**d**). **e**, **f**, Calculated Co L_3/L_2 area ratio (**e**) and O/Co ratio (**f**) of cycled P-LCO and La-LCO from (**c**, **d**). **g**, **h**, HRTEM near the surfaces of cycled P-LCO (**g**) and La-LCO (**h**), showing the CEI layer enclosed by dash lines. Scale bars: 5 nm (**a**, **b**, **g**, **h**). **i**–**l**, XPS of C 1*s* (**i**, **k**) and F 1*s* (**j**, **l**) for cycled P-LCO (**i**, **j**) and La-LCO (**k**, **l**). Details for XPS analysis are listed in Supplementary Table 5 and 6. Characterizations in (**a**–**l**) were conducted on samples after 100 cycles at 1 C and 3.0–4.6 V (vs. Li^+/Li) in half cells. **m**, Dissolved Co in the electrolytes after 100 and 200 cycles under 1 C within 3.0–4.6 V (vs. Li^+/Li) in half cells. **n**, **o**, XPS of Co 2*p* at the surface of the cycled graphite anodes in pouch cells using La-LCO (**n**) and P-LCO (**o**) cathodes after 200 cycles under 200 mA at full-cell voltages 3.0–4.5 V.

https://doi.org/10.1038/s41560-022-01179-3

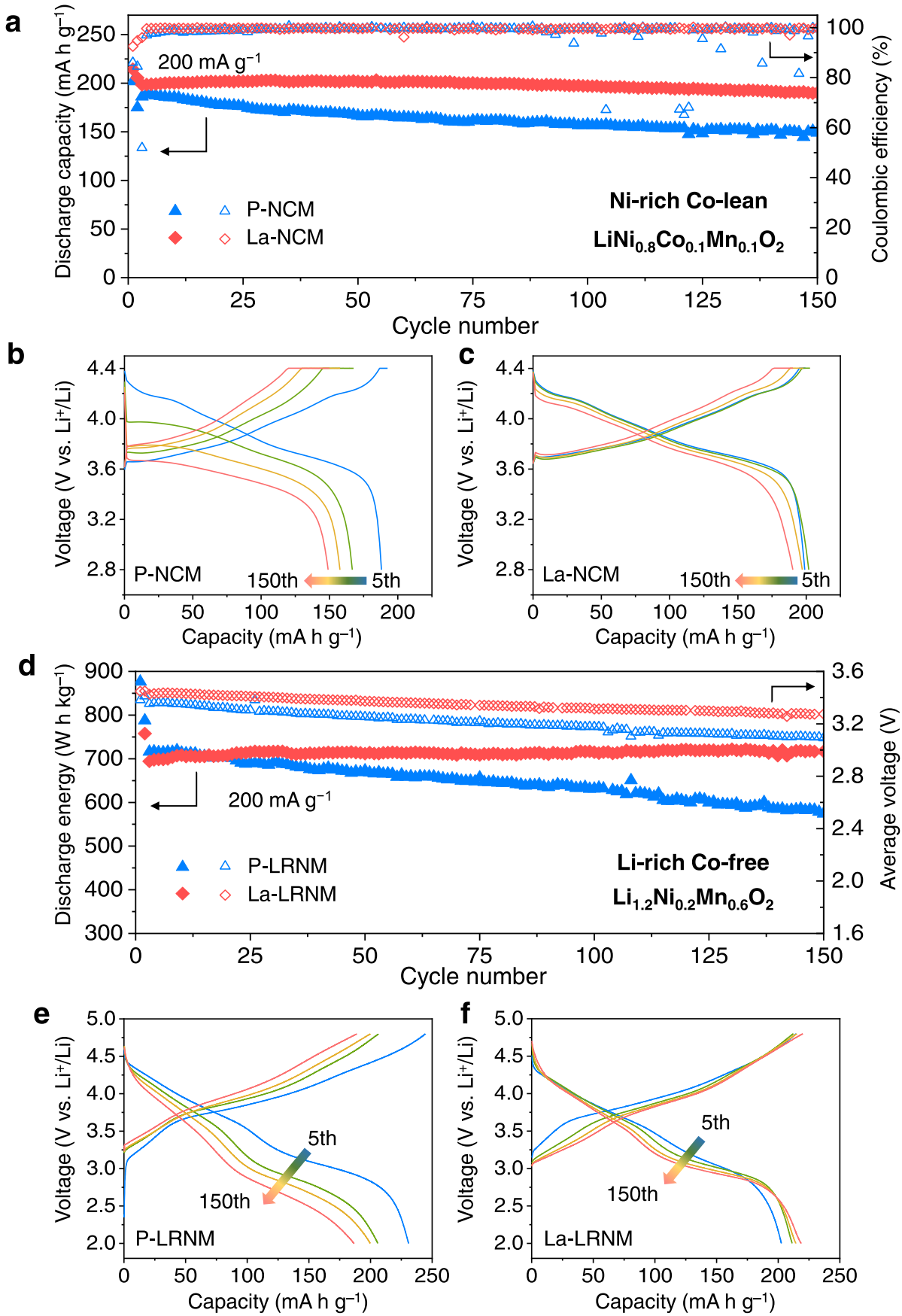

Extended Data Fig. 2 | Generalization of lanthurizing process to Co-lean NCM and Co-free LRNM cathodes. a, Cycling performance of P-NCM and La-NCM in coin-type half cells at 1 C at 2.8–4.4 V vs. Li^+/Li. **b, c**, Charge–discharge profiles of P-NCM (**b**) and La-NCM (**c**) at the 5^{th}, 50^{th}, 100^{th} and 150^{th} cycles. **d**, Cycling performance of P-LRNM and La-LRNM in coin-type half cells at 1 C at 2.0–4.8 V vs. Li^+/Li. **e, f**, Charge–discharge profiles of P-LRNM (**e**) and La-LRNM (**f**) at the 5^{th}, 50^{th}, 100^{th} and 150^{th} cycles.

nature energy

Article

https://doi.org/10.1038/s41560-022-01179-3

Stalling oxygen evolution in high-voltage cathodes by lanthurization

In the format provided by the authors and unedited

Supplementary Note 1: Suppressed surface phase transformations and CEI growth

Detailed structural and chemical characterizations were conducted on cycled P-LCO and La-LCO. For cycled P-LCO, we observed Moiré effects indicating lattice distortions and Co_3O_4-like phase near the surface of the oxide particle under HRTEM (**Extended Data Figure 1a**). In comparison, the lattice of cycled La-LCO is more ordered, and the near-surface $LiCoO_2$ lattice remains layered (**Extended Data Figure 1b**). Using EELS (**Extended Data Figure 1c** and **1d**, scanning directions in **Supplementary Figure 17**), we found defective oxygen sublattice and mixed Co^{2+}/Co^{3+} at the surface of cycled P-LCO, indicating oxygen loss and transition metal reduction. In comparison, the cycled La-LCO show well-preserved oxygen sublattice and no Co^{2+} signals. We further quantified the Co L_3/L_2 peak ratio and O/Co ratio for cycled P-LCO and La-LCO at the function of the distance to the surface[1,2]. For cycled P-LCO, Co reduction can be clearly seen at 0-5 nm from the surface (**Extended Data Figure 1e**). This is consistent with the calculated O/Co ratio (**Extended Data Figure 1f**), which is less than 2.0 near the surface and decreases to 1.4 at 0 nm (close to 1.333 in Co_3O_4). For cycled La-LCO, instead of decreasing, the average Co valence and O/Co ratio increases from the bulk to the surface, which is consistent with the chemical state (mixed Co^{3+}/Co^{4+}) and composition (O/Co ratio of 2.88 in $La_{0.76}Ca_{0.24}CoO_{2.88}$) before cycling.

Outside of the oxide particles, CEIs are known to form due to side reactions between the cathode-active material and the organic electrolyte. Under HRTEM, we observed a thinner and more uniform CEI layer in cycled La-LCO (**Extended Data Figure 1h**) than that in cycled P-LCO (**Extended Data Figure 1g**). Such observations are consistent with the particle surface morphologies under SEM (**Supplementary Figure 18**), which shows more side-reaction derived residues at the surface of cycled P-LCO than of cycled La-LCO. The chemical compositions of the CEIs were analyzed by XPS. We found stronger C 1*s* signals at the surface of the cycled P-LCO (**Extended Data Figure 1i**) than the cycled La-LCO (**Extended Data Figure 1j**). In contrast, F 1*s* signals are stronger for La-LCO than for P-LCO. Quantitative analysis (**Supplementary Table 7**) shows the CEIs of cycled La-LCO contains more F (43 at%), O (20 at%), and P (4 at%) and less C (33 at%) than those of cycled P-LCO (28 at% F, 11 at% O, 2 at% P, and 59 at% C). For high-voltage cathodes, lithium salt-derived F-rich inorganic CEI components such as LiF and $Li_xF_yPO_z$ are known to be stable and improve the cycling stability, while solvent-derived organic C-rich components are less stable[3,4]. (Detailed analysis on C 1*s* and F 1*s* signals are given in **Supplementary Table 8** and

9, respectively.) Therefore, we conclude that better CEIs form and less side reactions take place at the surface of La-LCO, which also contributes to the superior cycling performance.

The dissolved Co could migrate to and be deposited on the anode, which degrades the battery. We thus measured the dissolved Co in the electrolytes of the cycled cells by ICP-OES (**Extended Data Figure 1m**). For the cells using P-LCO cathode, the cycled electrolytes contain 94.30 ppm and 140.77 ppm Co after 100 and 200 cycles, respectively. In comparison, the electrolytes in the cells using La-LCO contain much less dissolved Co (6.07 ppm after 100 cycles and 6.85 ppm after 200 cycles). This is consistent with the trends in Co deposition on graphite anodes in pouch cells: Co signals can be clearly detected by XPS at the surface of cycled graphite anode when using P-LCO (**Extended Data Figure 1o**), while they are absent in cells using La-LCO (**Extended Data Figure 1n**).

To characterize the structural evolution during electrochemical cycling, we conducted in-situ XRD for the first two cycles. **Supplementary Figure 19** shows the evolution of (003) peak (full XRD spectra in **Supplementary Figure 20**). O3-O1 phase transformation and lattice breathing can be observed in both samples. This is consistent with logic that surface modifications should not affect the bulk behaviors. However, we found that after cycling, the (003) peak of P-LCO cannot move back to its original position (circled in dash lines in **Supplementary Figure 19b**) in the fully discharged state at 3.0 V vs. Li^+/Li. It indicates irreversible structural change in cycled P-LCO. The results suggest coupled electrochemical and structural degradations. Apparently, good surface passivation and suppresses oxygen loss and surface side reactions improve the structural reversibility, which is the reason why (003) peak of La-LCO can move back to its original position after cycling while that of P-LCO cannot.

Supplementary Note 2: Generalization to Co-lean/free cathodes

For sustainable battery development, there is a growing interest in Co-lean and Co-free cathodes such as NCM and LRNM. Considering the similarities among perovskite-type conductive ceramics $LaCoO_3$, $LaNiO_3$, and $LaMnO_3$[5], we expect our lanthurizing process to be applicable to these cathodes based on Ni or hybrid Ni-O redox chemistry. Since NCM and LRNM are sensitive to water, we chose N,N-dimethylformamide (DMF), an aprotic solvent in place of water for the ion exchange to suppress surface lithium extraction, phase transformation and Mn dissolution during synthesis.

For Ni-rich layered cathode, we found that the lanthurized NCM (La-NCM) has higher capacity and better cycling stability than the pristine NCM (P-NCM). When cycled between 2.8 V and 4.4 V (vs. Li^+/Li), La-NCM has a first-cycle CE of 92.5% (at 0.2 C, **Supplementary Figure 21**), 198 mAh g^{-1} discharge capacity at 1 C, 95.9% capacity retention after 150 cycles at 1 C, and an average CE of 99.5% (**Extended Data Figure 2a**), while P-NCM only has 86.0% first-cycle CE, 186 mAh g^{-1} discharge capacity at 1 C, 80.0% capacity retention, and 97.7% average CE, respectively. For La-NCM, the charge-discharge curves at 1 C remain stable at different cycles (**Extended Data Figure 2c**), while rapid degradation occurs for P-NCM (**Extended Data Figure 2b**).

For Co-free Li-/Mn-rich layered cathode, the lanthurized LRNM (La-LRNM) also shows better electrochemical performance than the pristine LRNM (P-LRNM). When cycled between 2.0 V and 4.8 V (vs. Li^+/Li) at 0.2 C, La-LRNM has a higher first-cycle CE of 83.3% than 76.9% for P-LRNM (**Supplementary Figure 22**). Since voltage decay is a major issue for Li-rich layered cathodes, we compared the discharge energy density (capacity times average voltage, on the cathode active material level) and average discharge voltage with or without our lanthurizing treatment. When cycled at 1 C, La-LRNM has a discharge energy density of 694.2 Wh kg^{-1} initially and 717.0 Wh kg^{-1} after 150 cycles with minimal decays and a slow voltage decay of 1.17 mV per cycle (**Extended Data Figure 2d**). In comparison, P-LRNM has 716.0 Wh kg^{-1} initially and 574 Wh kg^{-1} after 150 cycles (19.8% decay in energy density) and a faster voltage decay of 2.13 mV per cycle. (Cycling data of discharge capacity and CE available in **Supplementary Figure 23**.) It is accompanied by stable charge-discharge curves for La-LRNM (**Extended Data Figure 2f**) vs. fading ones for P-LRNM (**Extended Data Figure 2e**). These results demonstrate lanthurization as a general method

to construct high-energy-density cathodes with enhanced electrochemical performance, especially the high-voltage cycling stability.

Supplementary Note 3: Design strategy of surface perovskite phase

The general design strategy is to utilize the exchanged ion and the transition metal ion in the cathode (e.g., Co^{3+} in $LiCoO_2$) to form an epitaxial perovskite structure ABO_3 with oxygen deficiency (i.e., with oxygen vacancy). Since Ni^{3+}, Co^{3+}, $Mn^{3+/4+}$ can only be at B-site, we need to choose the proper A-site ions.

We used Goldschmidt tolerance factor $t=(r_A+r_O)/\mathrm{sqrt}(2)(r_B+r_O)$ to calculate the suitable crystal radius of A-site cation (12 coordinated) and Co^{3+} (6 coordinated, Shannon radius 68.5 pm) to form stable perovskite. For an appropriate t in the range from 0.78 to 1.05[6], we obtained that the ionic radius of A-site cation should be in the range of 88.5 pm to 162.8 pm. For charge balance, the major A-site cation should be +3. So lanthanide elements such as Pr^{3+} (146 pm), Gd^{3+} (141 pm), and Yb^{3+} (134 pm)[7] could be good candidates in addition to La^{3+} (150 pm). For minor divalent A-site cation, Ca^{2+} (148 pm) and Sr^{2+} (158 pm) could be good candidates.

In our experimental design, in addition to the perovskite formability, the divalent and trivalent cations need to the exchanged to the Li-site of $LiCoO_2$. So too large cations may experience some difficulties. We thus conducted additional experiments. For trivalent candidates, we found that Pr^{3+}, Gd^{3+}, and Yb^{3+} can work similar to La^{3+} and the electrochemical performance are shown in **Supplementary Figure 24**. For divalent candidates, we found that Sr^{2+} is too large to be ion-exchanged into the lattice of $LiCoO_2$ so Ca^{2+} remains as the choice for minor divalent doping.

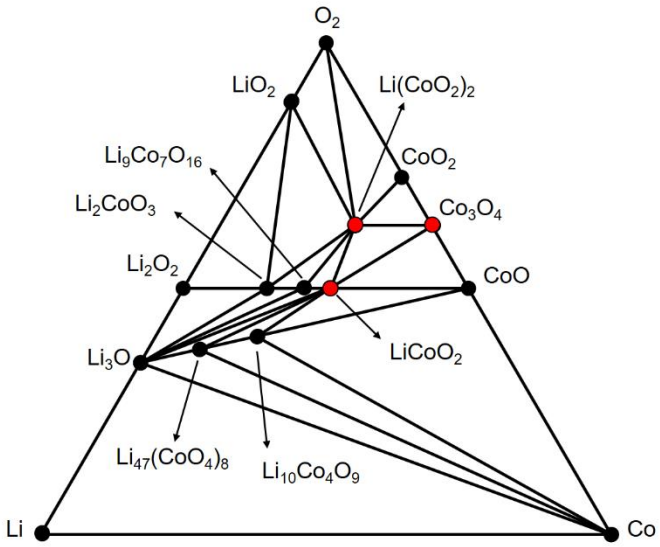

Supplementary Figure 1 | Li-Co-O ternary phase diagram computed by DFT at materialsproject.org[8,9].

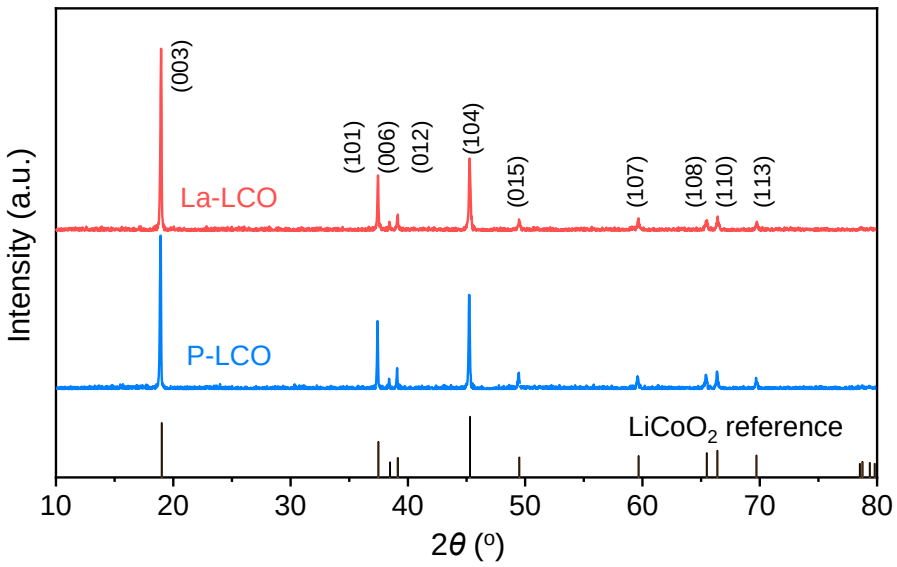

Supplementary Figure 2 | XRD patterns of P-LCO and La-LCO, and reference pattern of $LiCoO_2$ (PDF#50-0653).

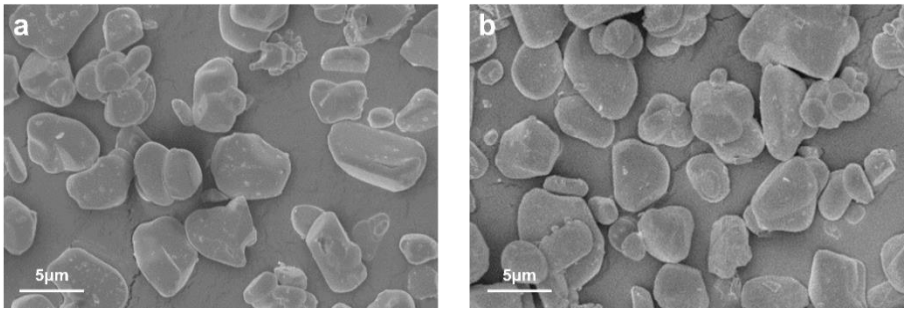

Supplementary Figure 3 | SEM of (a) P-LCO and (b) La-LCO.

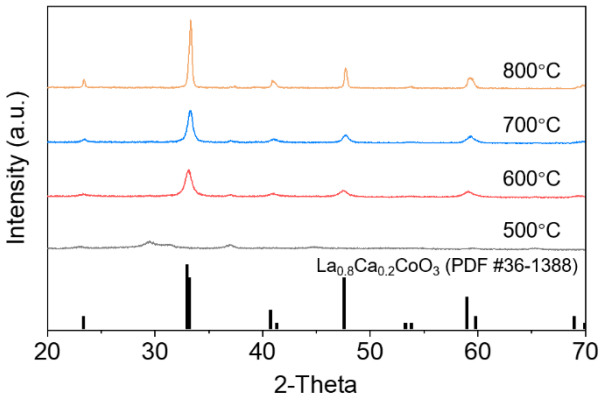

Supplementary Figure 4 | XRD patterns of $La_{0.8}Ca_{0.2}CoO_{3-\delta}$ synthesized by the sol-gel method and heat-treated at 500 °C, 600 °C, 700 °C, and 800 °C for 6 h.

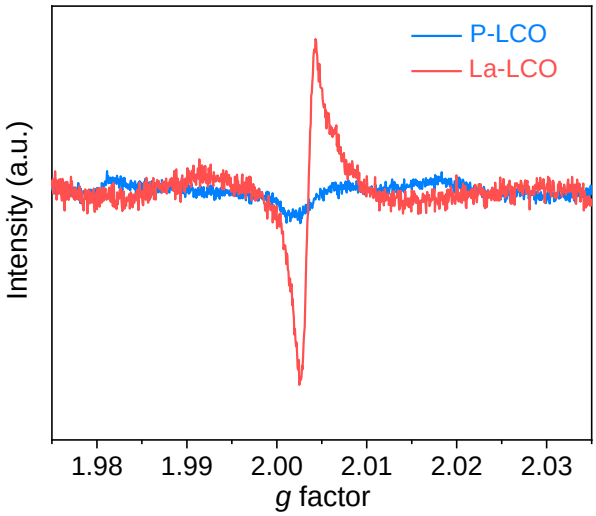

Supplementary Figure 5 | EPR spectra of P-LCO and La-LCO powders, indicating much higher concentration of oxygen vacancies in La-LCO than in P-LCO. EPR spectrum is sensitive to detect unpaired electrons, and the ones associated with oxygen vacancies have a *g* factor around 2.004. $LiCoO_2$ has a close-packed anion sublattice and a high oxygen vacancy formation energy, which agrees with our observation that a minimum amount of oxygen vacancies exists in P-LCO. Therefore, the extra amount of oxygen vacancies in La-LCO is attributed to the non-stoichiometric perovskite surface layer.

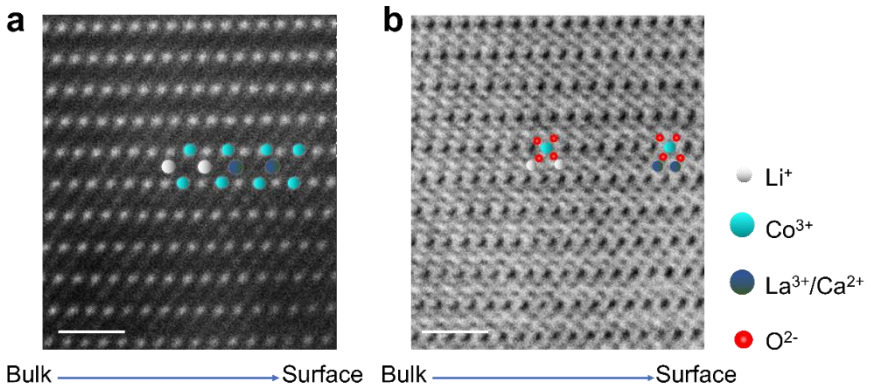

Supplementary Figure 6 | (a) STEM-HAADF image and (b) the corresponding annular bright-field mode (ABF) image of the Region II in La-LCO. Scale bars: 1 nm. The occupied positions of the different atoms were marked, which indicating distinguishing variation of Co-O distance from bulk (shorter Co-O distance and smaller CoO6 "void" in ABF) to surface (longer Co-O distance and larger CoO_6 "void" in ABF).

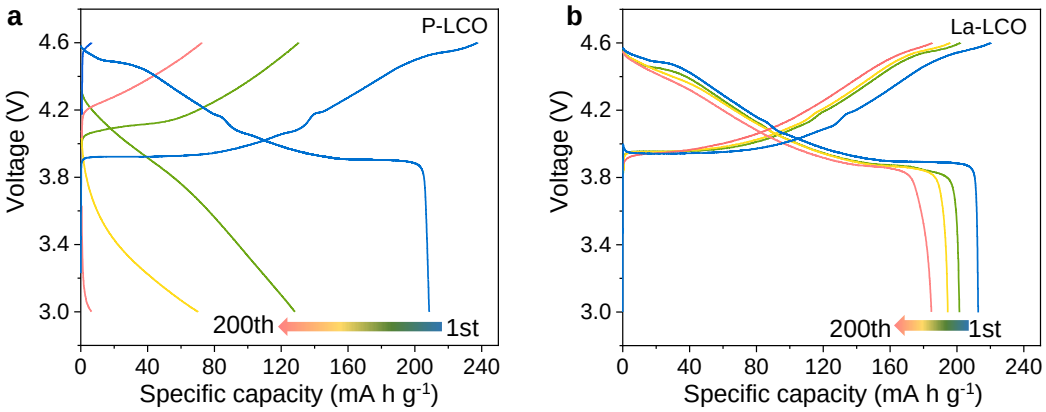

Supplementary Figure 7 | Charge-discharge profiles of (a) P-LCO and (b) La-LCO within 3.0-4.6 V at 1st, 50th, 100th and 200th cycles in coin-type half cells. Same cycling conditions as **Figure 4b**.

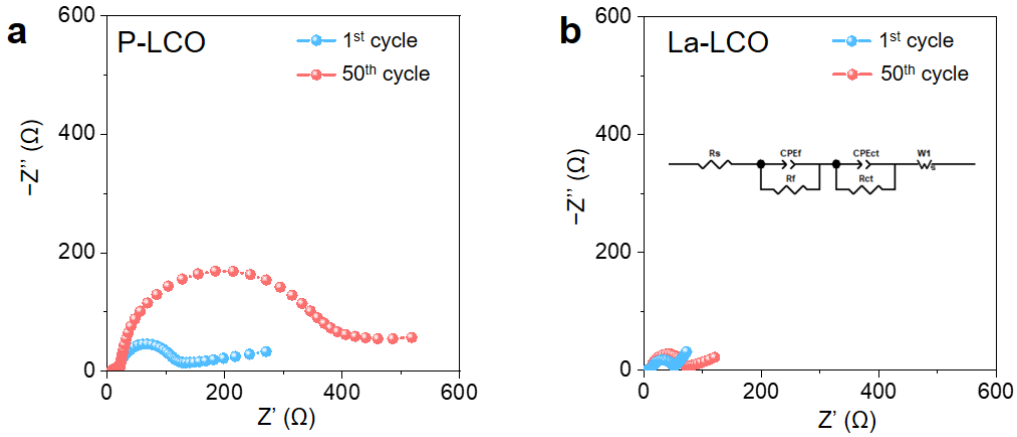

Supplementary Figure 8 | EIS data of (a) P-LCO and (b) La-LCO at 4.6 V vs. Li^+/Li in the 1st and 50th cycle. Z' and Z'' denote the real and imaginary parts of the complex impedance, respectively. Cycling conditions: 1 C at 3.0-4.6 V vs. Li^+/Li. Equivalent circuit shown in the inset of **Supplementary Figure 8b**.

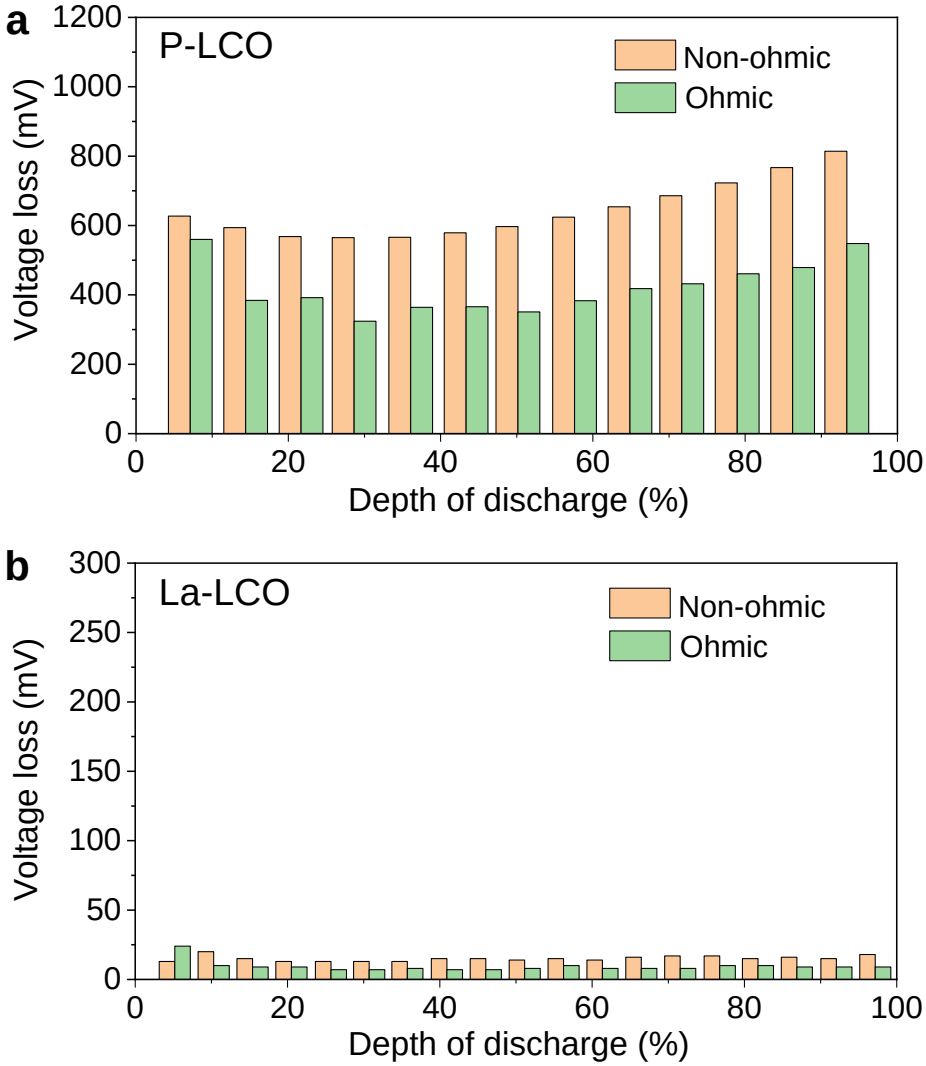

Supplementary Figure 9 | Voltage losses (as a function of depth of discharge and separated as ohmic and non-ohmic losses) of (a) P-LCO and (b) La-LCO from GITT measurements (conducted with a titration current of 0.2 C, a titration time of 15 min and a relaxation time of 1 h) after the 50th discharge cycle at 1 C and 3.0-4.6 V vs. Li^+/Li.

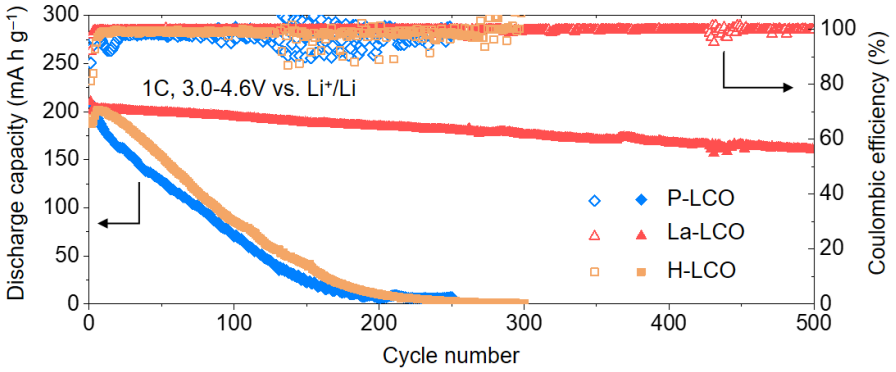

Supplementary Figure 10 | Cycling performance of P-LCO, La-LCO, and H-LCO. Cycling conditions: 1 C for both charge and discharge at 3.0-4.6 V (vs. Li^+/Li).

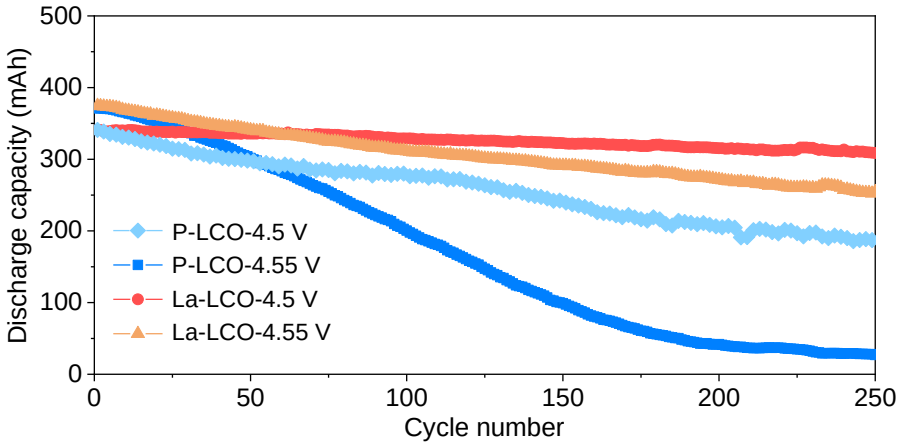

Supplementary Figure 11 | Comparison of discharge capacities of P-LCO and La-LCO in pouch-type full cells cycled at 200 mA and between 3.0 V and different upper cutoff voltages (4.5 V or 4.55 V).

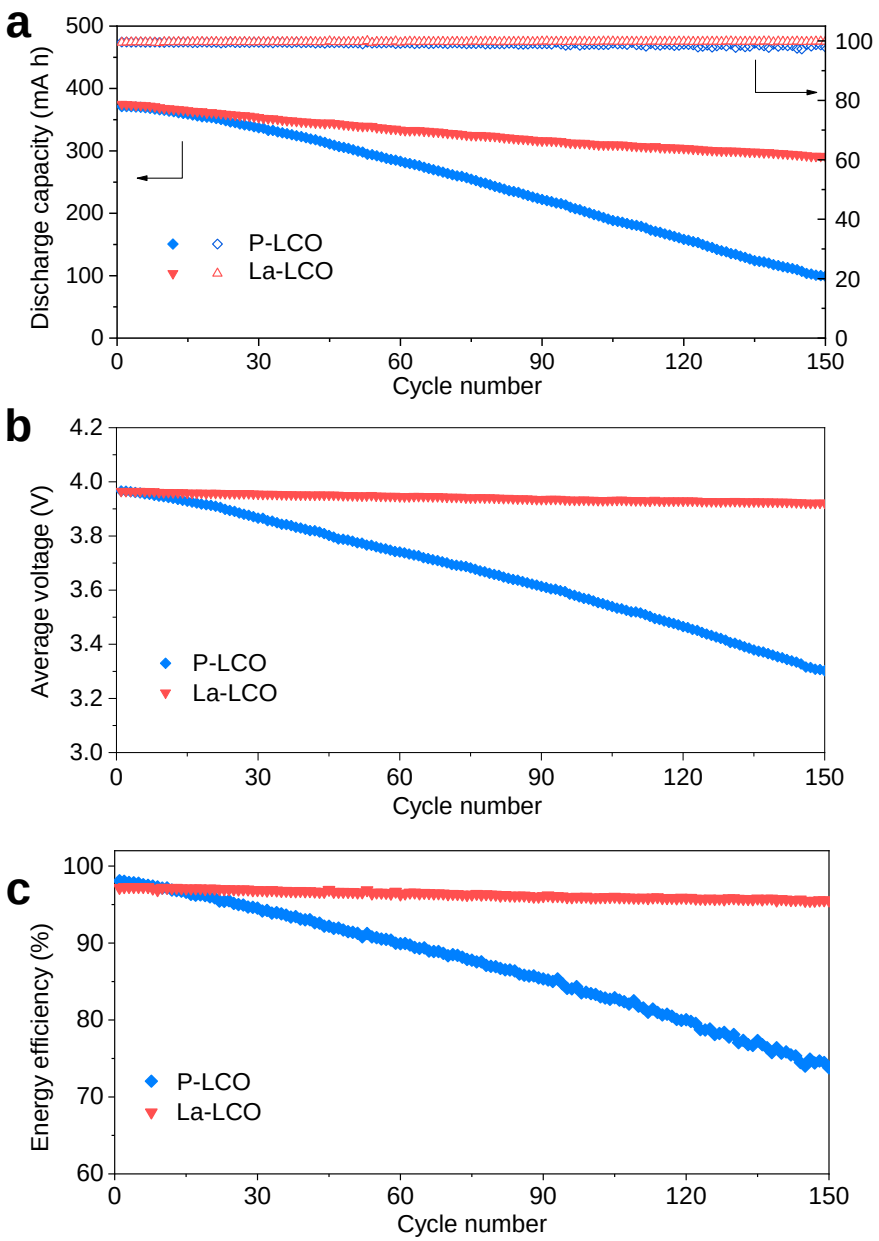

Supplementary Figure 12 | (a) Discharge capacity, (b) average voltage, and (c) energy efficiency of P-LCO and La-LCO in the voltage range of 3.0-4.55 V in pouch-type full cells.

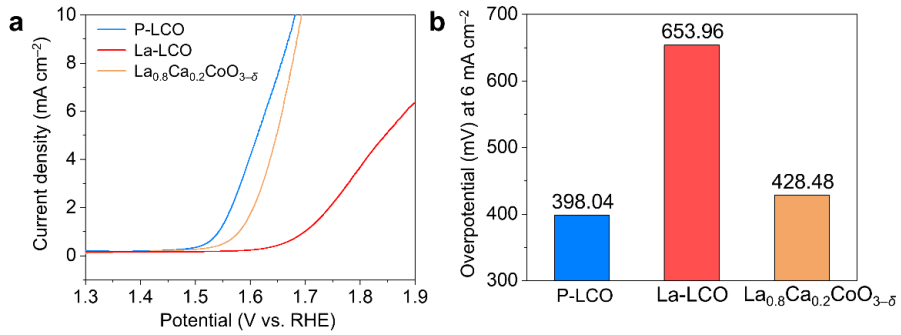

Supplementary Figure 13 | OER electrocatalytic performance for of P-LCO, La-LCO, and $La_{0.8}Ca_{0.2}CoO_{3-\delta}$ in 0.1 M KOH aqueous solution at room temperature. (a) Linear sweep voltammetry (LSV) curves at a scan rate of 10 mV s^{-1}. Voltages are vs. reversible hydrogen electrode (RHE). (b) Measured overpotential at 6 mA cm^{-2} current density.

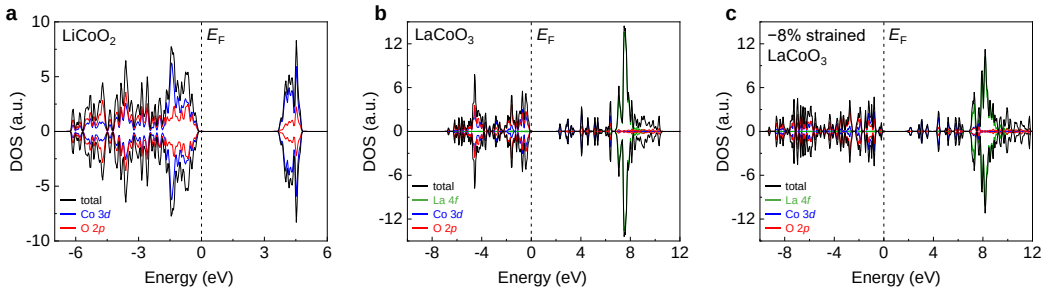

Supplementary Figure 14 | Total and projected DOS of (a) $LiCoO_2$, (b) unstrained $LaCoO_3$, and (c) −8% strained $LaCoO_3$.

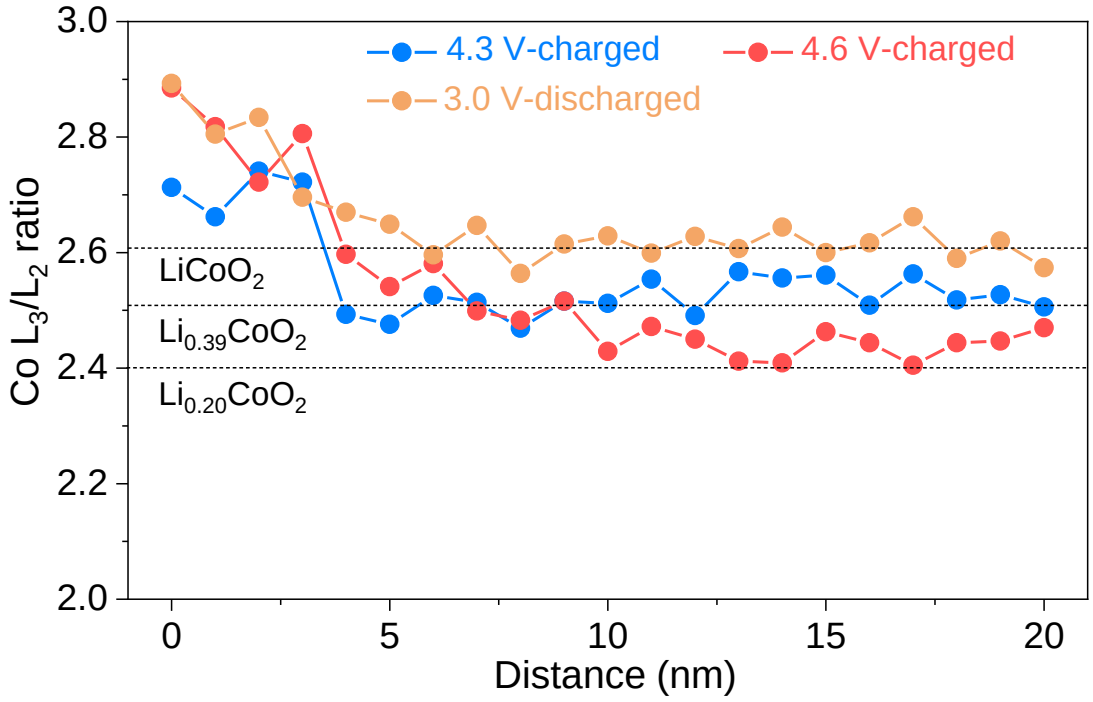

Supplementary Figure 15 | Calculated Co L_3/L_2 area ratio for P-LCO under different charge states (4.3 V-charged, 4.6 V-charged, and 3.0 V-discharged). Dash lines are referred Co states from La-LCO in Fig. 5j.

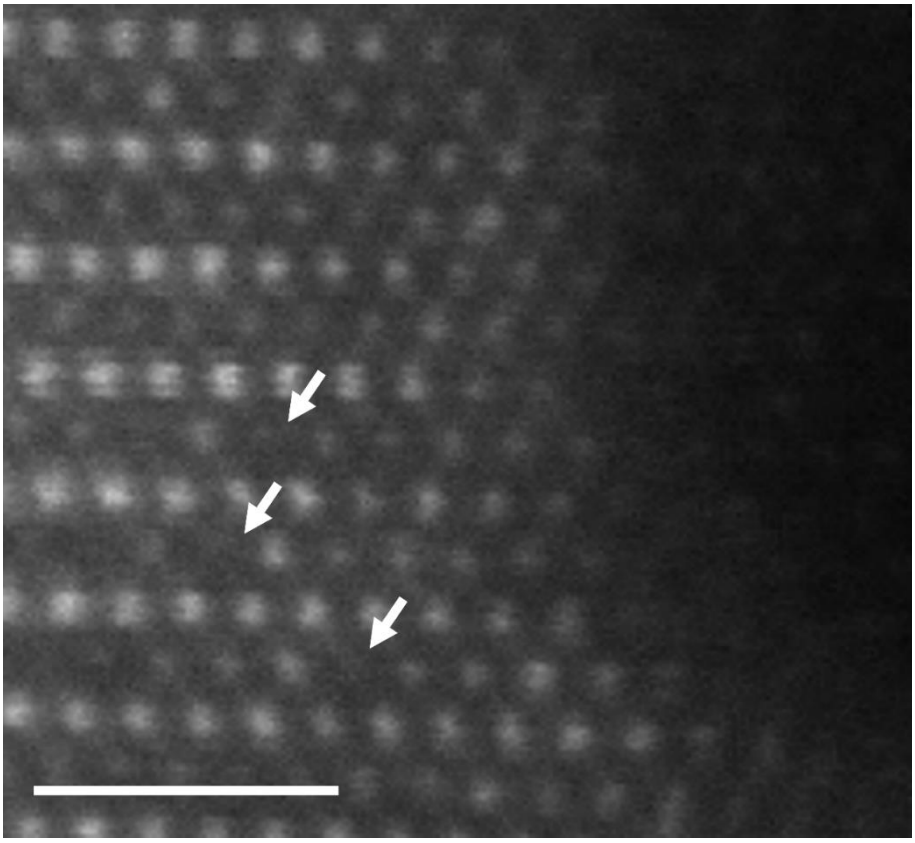

Supplementary Figure 16 | HAADF-STEM image at the surface of La-LCO. Arrows point to lattice sites with weak contrasts, indicating the existence of Li doping in the surface phase. Scale bar: 1 nm.

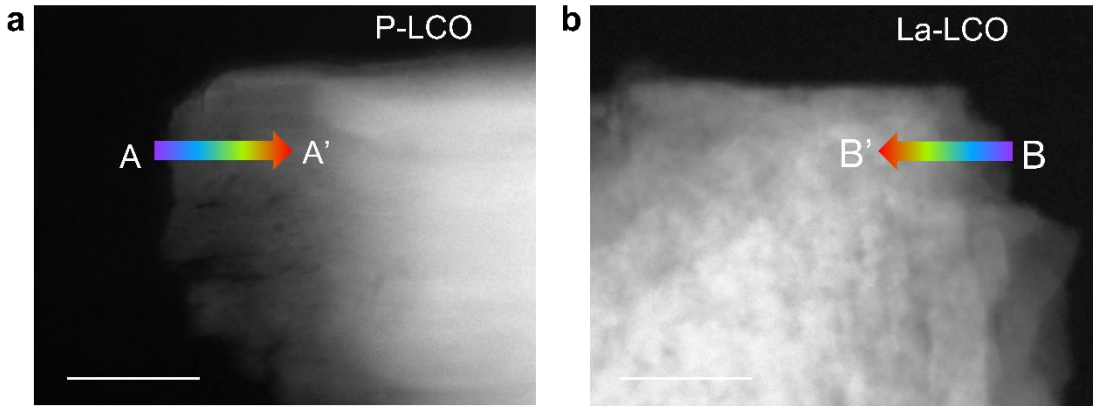

Supplementary Figure 17 | Low-magnification HAADF-STEM images of (a) P-LCO and (b) La-LCO after 100 cycles at 1 C and 3.0-4.6 V vs. Li^+/Li. Rainbow-colored arrows denote directions for EELS line profiling in **Extended Data Figure 1c-f**. Scale bars: 50 nm.

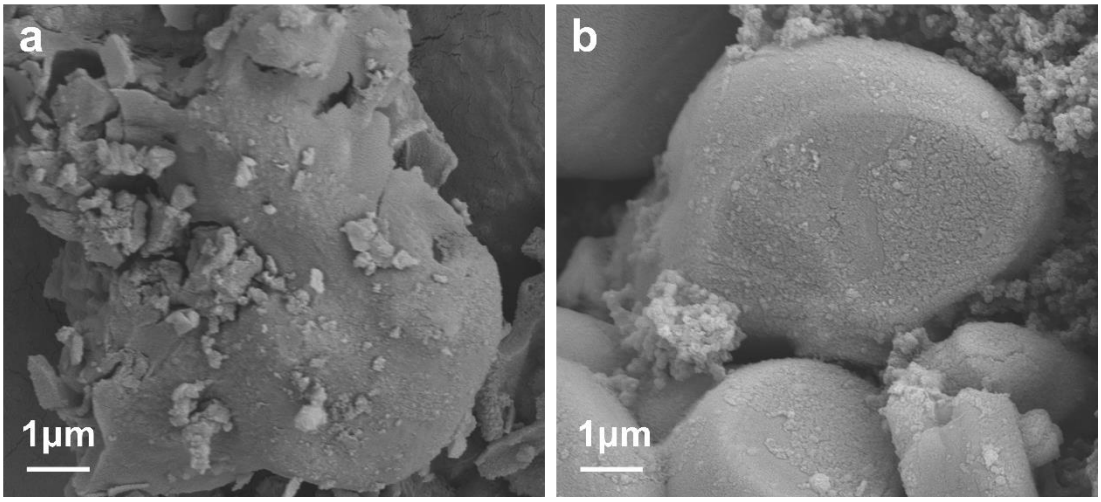

Supplementary Figure 18 | SEM of (a) P-LCO and (b) La-LCO after 100 cycles at 1 C and 3.0-4.6 V vs. Li^+/Li.

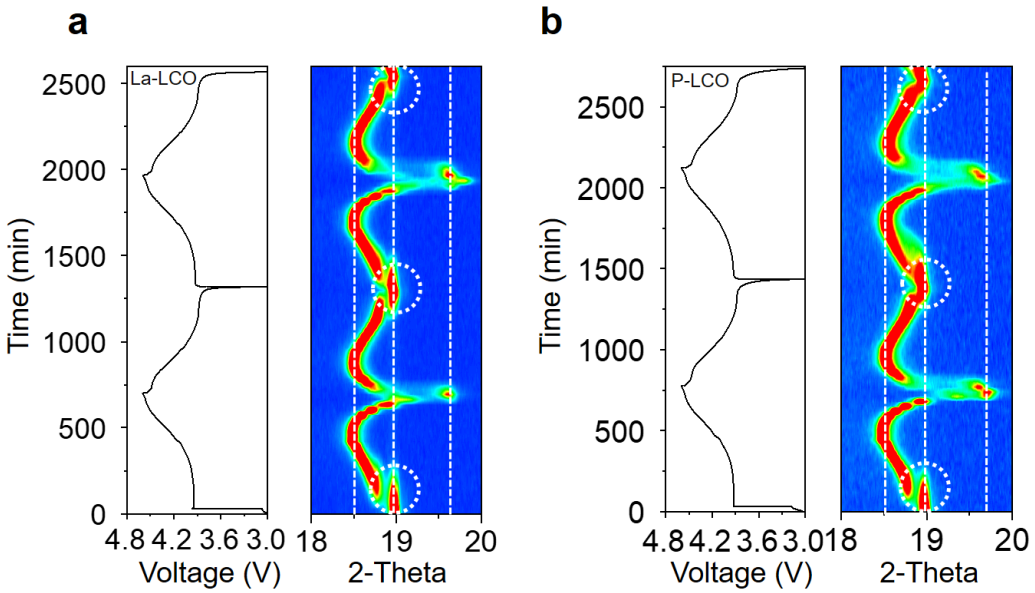

Supplementary Figure 19 | In-situ XRD patterns around (003) peak of P-LCO and La-LCO collected in the first two cycles in 3.0-4.6 V (vs. Li^+/Li) at 0.1 C.

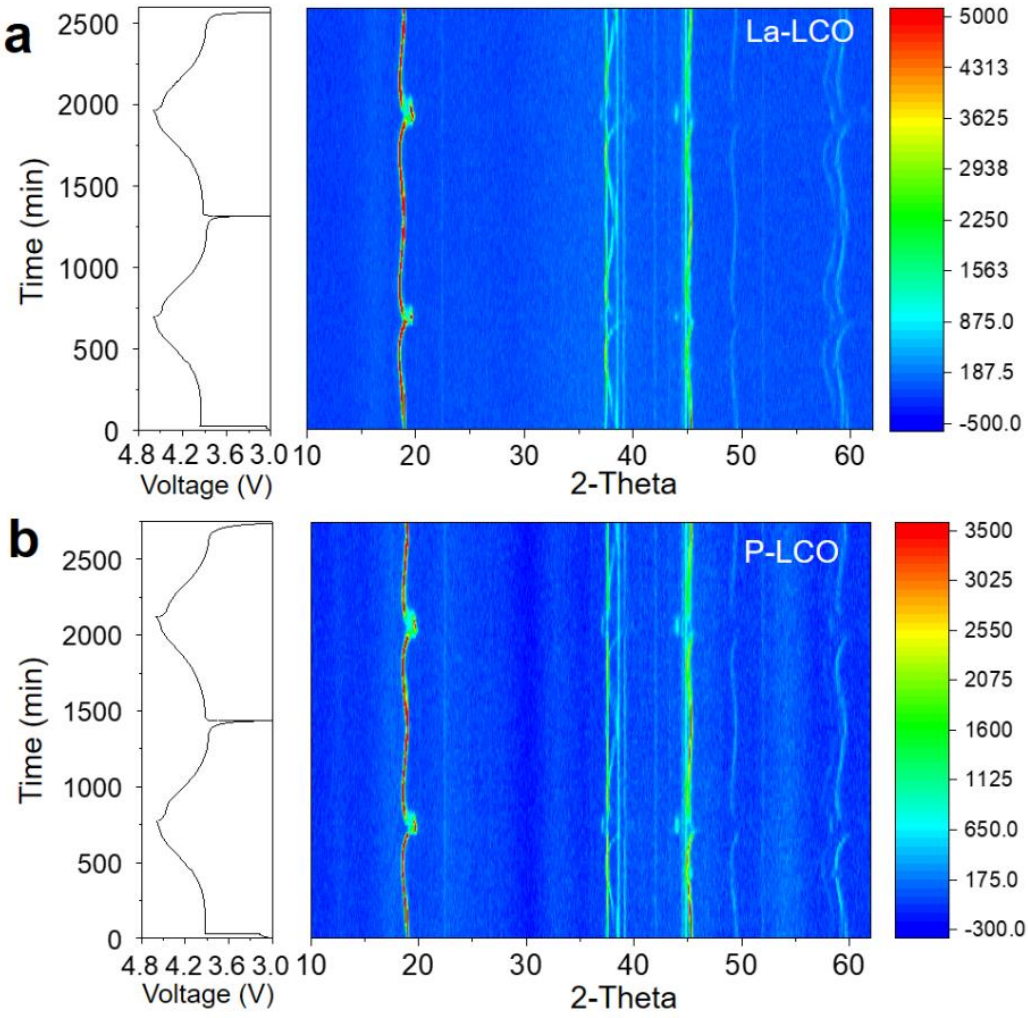

Supplementary Figure 20 | In-situ XRD patterns (full range) of P-LCO and La-LCO collected in the first two cycles in 3.0-4.6 V (vs. Li^+/Li) at 0.1 C.

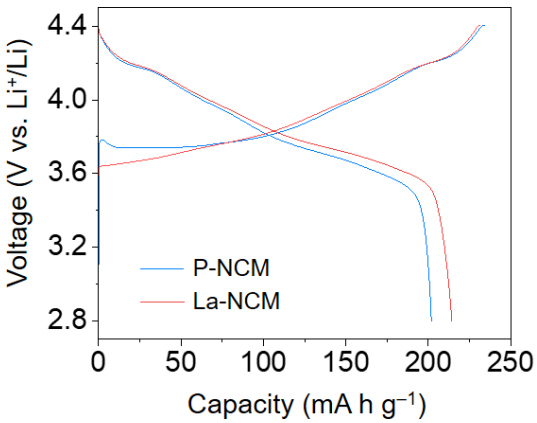

Supplementary Figure 21 | Charge-discharge curves of P-NCM and La-NCM during 1st cycle at 0.2 C within 2.8-4.4 V (V vs. Li^+/Li).

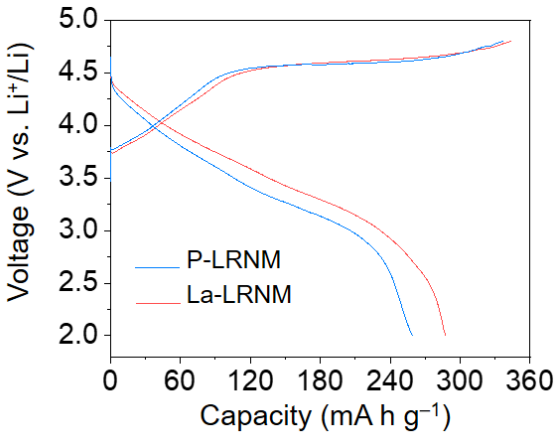

Supplementary Figure 22 | GCD curves of P-LRNM and La-NCM during 1st cycle within 2-4.8 V (V vs. Li^+/Li).

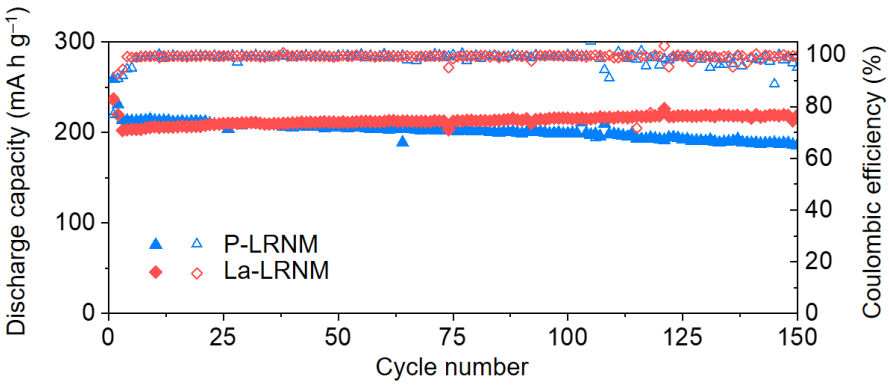

Supplementary Figure 23 | Cycling performance of P-LRNM and La-LRNM in the voltage range of 2.0-4.8 V at 1C.

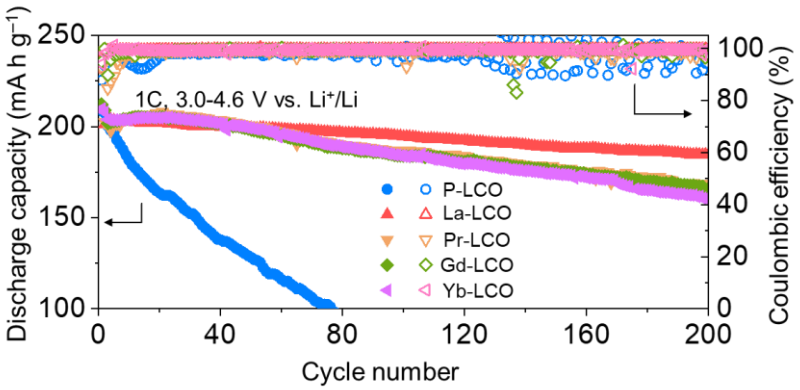

Supplementary Figure 24 | Cycling performances of La-LCO, Pr-LCO, Gd-LCO, Yb-LCO and P-LCO at 1 C in the voltage range of 3.0-4.6 V vs. Li^+/Li. Here Pr-LCO, Gd-LCO, and Yb-LCO were similarly synthesized to La-LCO, with the same ion concentrations, and the ion-exchange and heat-treatment conditions.

Supplementary Table 1 | La and Ca concentrations (measured by ICP-OES) in La-LCO. The data show outward-exchanged Li^+ in the treated aqueous solution; Co dissolution is minimal according to the data.

Element	La	Ca
Weight ($\mu g\ mL^{-1}$)	11.023	0.989
mol% per mol $LiCoO_2$	0.234	0.072

Supplementary Table 2 | Quantity of Li and Co (measured by ICP-OES) in the treated $LaCl_3$ and $CaCl_2$ solution after the ion-exchange step.

Concentration (M) of $LaCl_3$ and $CaCl_2$	Weight of Li (μg mL^{-1})	Weight of Co (μg mL^{-1})	Out-exchanged Li (mol%) per mol $LiCoO_2$	Out-exchanged Co (mol%) per mol $LiCoO_2$
0.16	69.81	35.28	0.2963	0.0176
0.4	156.74	61.77	0.6652	0.0309
0.8	337.08	120.45	1.4306	0.0602

Supplementary Table 3 | Fitting results of the EIS data in **Supplementary Figure 8**.

	P-LCO		La-LCO	
	1st cycle	50th cycle	1st cycle	50th cycle
R_s (Ω)	8.9	6.8	7.4	7.6
R_f (Ω)	9.9	13.8	7.5	11.0
R_{ct} (Ω)	103.3	377.8	39.6	61.6

Supplementary Table 4 | Comparison of cycling performance of 4.5 V (vs. Li^+/Li) $LiCoO_2$ in the literature.

Modification strategy	Rate (mA g^{-1})	Capacity	Retention	Ref.
Lathurized $LiCoO_2$	200	179.7 mA h g^{-1} after 600 cycles	97.9% after 600 cycles	This work
La, Al co-doped $LiCoO_2$	27.4	182.4 mAh g^{-1} after 50 cycles	96% after 50 cycles	10
Al/Ti bulk-doped and Mg surface-doped $LiCoO_2$	140	164.5 mAh g^{-1} after 200 cycles	77% after 200 cycles	11
Al-doped ZnO-coated $LiCoO_2$	37	141.4 mAh g^{-1} after 650 cycles	80% after 650 cycles	12
Phosphate-coated and Mn-doped $LiCoO_2$	140	151.5 mAh g^{-1} after 700 cycles	83.7% after 700 cycles	13
Nano-Ag embedded $LiCoO_2$	100	155 mAh g^{-1} after 100 cycles	82% after 100 cycles	14
$Li_{1.4}Al_{0.4}Ti_{1.6}(PO_4)_3$-coated $LiCoO_2$	300	163.9 mAh g^{-1} after 100 cycles	93.1% after 100 cycles	15

Supplementary Table 5 | Comparison of cycling performance of 4.6 V (vs. Li^+/Li) $LiCoO_2$ in the literature.

Modification strategy	Rate ($mA\ g^{-1}$)	Capacity	Retention	Ref.
Lathurized $LiCoO_2$	200	195 mA h g^{-1} after 100 cycles, 185 mA h g^{-1} after 200 cycles, 177 mA h g^{-1} after 300 cycles, 168 mA h g^{-1} after 400 cycles, 166 mA h g^{-1} after 500 cycles	96.7% after 100 cycles, 91.8% after 200 cycles, 87.9% after 300 cycles, 83.4% after 400 cycles, 79.8% after 500 cycles	This work
$AlPO_4$ coated $LiCoO_2$	140	150 mA h g^{-1} after 50 cycles	64.3% after 50 cycles	16
$LiAlO_2$ coated $LiCoO_2$	50	172 mA h g^{-1} after 50 cycles	76.9% after 50 cycles	17
Hydrothermal assisted Li/Al/F-modified $LiCoO_2$	27.4	171 mA h g^{-1} after 200 cycles	82.2% after 200 cycles	18
Ti/Al/Mg co-doped $LiCoO_2$	137	174 mA h g^{-1} after 100 cycles	86% after 100 cycles	19
Al/Ti bulk-doped and Mg surface-doped $LiCoO_2$	137	170 mA h g^{-1} after 200 cycles	80.2% after 200 cycles	11
$LiMn_{1.5}Ni_{0.5}O_4$ coated $LiCoO_2$	50	182 mA h g^{-1} after 100 cycles	80.0% after 200 cycles	20
AlZnO coated $LiCoO_2$	185	121 mA h g^{-1} after 500 cycles	65.7% after 500 cycles	21
LATP coated $LiCoO_2$	137	180 mA h g^{-1} after 100 cycles	85.8% after 100 cycles	4
Li_3PO_4 and $AlPO_4$ co-modified $LiCoO_2$	137	180 mA h g^{-1} after 200 cycles	84.3% after 200 cycles	16
Se surface-doped $LiCoO_2$	70	189 mA h g^{-1} after 120 cycles	86.7% after 120 cycles	22
Trace SO_2 in-situ modified LCO	280	176 mA h g^{-1} after 100 cycles	88% after 100 cycles	23
Al and F gradient-doped LCO	100	170.8 mA h g^{-1} after 100 cycles	86.9% after 200 cycles	24
Li-Al-PO_4 coated LCO	137	180.4 mA h g^{-1} after 200 cycles	88.6 after 200 cycles	25
MgF_2 doped LCO	270	184 mA h g^{-1} after 200 cycles	92% after 100 cycles	26
$LiAlH_4$ treated LCO	190	143.7 mA h g^{-1} after 500 cycles	71.6% after 500 cycles	27

Supplementary Table 6 | Apparent electrical conductivity of powders compacts of synthesized $La_{0.8}Ca_{0.2}CoO_{3-\delta}$, P-LCO, and La-LCO. The powders were pressed into pellets at 18 MPa at room temperature and heat-treated at 600 °C for 4 h to increase density. Electronic conductivity was measured by a linear sweep voltammetry. The apparent electrical conductivity is lower than the intrinsic bulk one due to porosities in the powder compacts.

Materials	$La_{0.8}Ca_{0.2}CoO_{3-\delta}$	P-LCO	La-LCO
Apparent electrical conductivity (S cm^{-1})	0.112	2.69×10^{-5}	2.75×10^{-4}

Supplementary Table 7 | XPS fitting results for the CEI element compositions of La-LCO and P-LCO after 100 cycles at 1 C and 3.0-4.6 V vs. Li^+/Li.

Element	C (at%)	O (at%)	F (at%)	P (at%)
P-LCO	59	11	28	2
La-LCO	33	20	43	4

Supplementary Table 8 | XPS fitting results for C 1*s* signals of La-LCO and P-LCO after 100 cycles at 1 C and 3.0-4.6 V vs. Li^+/Li.

C 1*s* XPS	Binding energy (eV)	Attributed group	Proportion (%)
P-LCO	291.25	F-C-F	19.1
	289.40	CO_3	2.6
	286.66	O-C=O	41.7
	285.20	C-O	9.6
	284.46	C-C	27.0
La-LCO	291.46	F-C-F	19.0
	289.55	CO_3	5.4
	286.90	O-C=O	48.4
	285.27	C-O	15.8
	284.50	C-C	11.4

Supplementary Table 9 | XPS fitting results for F 1*s* signals of La-LCO and P-LCO after 100 cycles at 1 C and 3.0-4.6 V vs. Li^+/Li.

F 1*s* XPS	Binding energy (eV)	Attributed group	Proportion (%)
P-LCO	688.35	$Li_xF_yPO_z$	77.1
	685.66	LiF	22.9
La-LCO	688.12	$Li_xF_yPO_z$	72.5
	685.65	LiF	27.5

Supplementary references

1. Wang, Z., Yin, J. & Jiang, Y. EELS analysis of cation valence states and oxygen vacancies in magnetic oxides. *Micron* **31**, 571–580 (2000).
2. Kikkawa, J., Terada, S., Gunji, A., Nagai, T., Kurashima, K. & Kimoto, K. Chemical states of overcharged $LiCoO_2$ particle surfaces and interiors observed using electron energy-loss spectroscopy. *J. Phys. Chem. C* **119**, 15823–15830 (2015).
3. Xue, W., *et al.* Ultra-high-voltage Ni-rich layered cathodes in practical Li metal batteries enabled by a sulfonamide-based electrolyte. *Nat. Energy* **6**, 495-505 (2021).
4. Wang, Y. *et al.* An in situ formed surface coating layer enabling $LiCoO_2$ with stable 4.6 V high-voltage cycle performances. *Adv. Energy Mater.* **10**, 2001413 (2020).
5. Suntivich, J., May, K. J., Gasteiger, H. A., Goodenough, J. B. & Shao-Horn, Y. A perovskite oxide optimized for oxygen evolution catalysis from molecular orbital principles. *Science* **334**, 1383–1385 (2011).
6. Randall, C. A., Bhalla, A. S., Shrout, T. R., & Cross, L. E. Classification and consequences of complex lead perovskite ferroelectrics with regard to B-site cation order. *J. Mater. Res.* **5**, 829-834 (1990).
7. Jia, Y. Q. Crystal radii and effective ionic radii of the rare earth ions. *J. Solid State Chem.* **95**, 184-187 (1991).
8. Ong, S. P., Wang, L., Kang, B. & Ceder, G. Li-Fe-P-O_2 phase diagram from first principles calculations. *Chem. Mater.* **20**, 1798−1807 (2008).
9. Ong, S. P., Jain, A., Hautier, G., Kang, B. & Ceder, G. Thermal stabilities of delithiated olivine MPO_4 (M= Fe, Mn) cathodes investigated using first principles calculations. *Electrochem. Commun.* **12**, 427−430 (2010).
10. Liu, Q., Su, X., Lei, D., Qin, Y., *et al.* Approaching the capacity limit of lithium cobalt oxide in lithium ion batteries via lanthanum and aluminum doping. *Nat. Energy* **3**, 936-943 (2018).
11. Wang, L. *et al.* A novel bifunctional self-stabilized strategy enabling 4.6 V $LiCoO_2$ with excellent long-term cyclability and high-rate capability. *Adv. Sci.* **6**, 1−11 (2019).
12. Nie, K., Sun, X., Wang, J., *et al.* Realizing long-term cycling stability and superior rate performance of 4.5 V-$LiCoO_2$ by aluminum doped zinc oxide coating achieved by a simple wet-mixing method. *J. Power Sources* **470**, 228423 (2020).
13. Gu, R., Qian, R., Lyu, Y., & Guo, B. One-step integrated commodification to improve the electrochemical performances of high-voltage $LiCoO_2$ for lithium-ion batteries. *ACS Sustain. Chem. Eng.* **8**, 9346-9355 (2020).
14. Meng, E., Jin, B., Hu, Y., Gong, F., Zhang, Y., & Jia, Q. Superior lithium ion storage performance of $LiCoO_2$ cathode at 4.5 V enabled by the multiple synergistic effect of nano-silver. *J. Electrochem. Soc.* **167**, 160516 (2020).
15. Yang, Q., Huang, J., Li, Y., *et al*. Surface-protected $LiCoO_2$ with ultrathin solid oxide electrolyte film for high-voltage lithium ion batteries and lithium polymer batteries. *J. Power Sources* **388**, 65-70 (2018).
16. Cho, J. *et al.* Comparison of Al_2O_3-and $AlPO_4$-coated $LiCoO_2$ cathode materials for a Li-ion cell. *J. Power Sources* **146**, 58−64 (2005).
17. Xie, J. *et al.* Engineering the surface of $LiCoO_2$ electrodes using atomic layer deposition for stable high-voltage lithium ion batteries. *Nano Res.* **10**, 3754−3764 (2017).

18. Qian, J. *et al.* Electrochemical surface passivation of $LiCoO_2$ particles at ultrahigh voltage and its applications in lithium-based batteries. *Nat. Commun.* **9**, 1−11 (2018).
19. Zhang, J. *et al.* Trace doping of multiple elements enables stable battery cycling of $LiCoO_2$ at 4.6 V. *Nat. Energy* **4**, 594−603 (2019).
20. Zhu, Z. *et al.* Gradient-morph $LiCoO_2$ single crystals with stabilized energy density above 3400 W h L^{-1}. *Energy & Environ. Sci.* **13**, 1865−1878 (2020).
21. Cheng, T. *et al.* Achieving stable cycling of $LiCoO_2$ at 4.6 V by multilayer surface modification. *Adv. Func. Mater.* **31**, 2001974 (2021).
22. Zhu, Z. *et al.* A surface Se-substituted $LiCo[O_{2-\delta}Se_{\delta}]$ cathode with ultrastable high-voltage cycling in pouch full-cells. *Adv. Mater.* **32**, 2005182 (2020).
23. Tan, X. *et al*. Simultaneous near-surface trace doping and surface modifications by gas-solid reactions during one-pot synthesis enable stable high-voltage performance of $LiCoO_2$. *Adv. Energy Mater.* **12**, 2200008 (2022).
24. Huang, W. *et al*. Surface design with cation and anion dual gradient stabilizes high-voltage $LiCoO_2$. *Adv. Energy Mater.* **12**, 2200813 (2022).
25. Wang, X. *et al*. Lithium-Aluminum-Phosphate coating enables stable 4.6 V cycling performance of $LiCoO_2$ at room temperature and beyond. *Energy Storage Mater.* **37**, 67−76 (2021).
26. Kong, W. *et al*. Tailoring Co3d and O2p band centers to inhibit oxygen escape for stable 4.6 V $LiCoO_2$ cathodes. *Angew. Chem. Int. Edit.* **133**, 27308-27318 (2021).
27. Wang, P. *et al*. Oxygen framework reconstruction by $LiAlH_4$ treatment enabling stable cycling of high-voltage $LiCoO_2$. *Energy Storage Mater.* **44**, 487−496 (2022).